



# Role of Copper Migration in Nanoscale Ageing of Supported CuO/Al<sub>2</sub>O<sub>3</sub> in Redox Conditions: A Combined Multiscale X-ray and Electron Microscopy Study

Sharmin Sharna, Virgile Rouchon, Christèle Legens, Anne-lise Taleb, Stefan Stanescu, Corinne Bouillet, Arnold Lambert, Valerie Briois, David Chiche, Anne-sophie Gay, et al.

## ► To cite this version:

Sharmin Sharna, Virgile Rouchon, Christèle Legens, Anne-lise Taleb, Stefan Stanescu, et al.. Role of Copper Migration in Nanoscale Ageing of Supported CuO/Al<sub>2</sub>O<sub>3</sub> in Redox Conditions: A Combined Multiscale X-ray and Electron Microscopy Study. ChemCatChem, 2023, 15 (4), pp.e202201259. 10.1002/cctc.202201259 . hal-04018381

**HAL Id: hal-04018381**

**<https://ifp.hal.science/hal-04018381>**

Submitted on 7 Mar 2023

**HAL** is a multi-disciplinary open access archive for the deposit and dissemination of scientific research documents, whether they are published or not. The documents may come from teaching and research institutions in France or abroad, or from public or private research centers.

L'archive ouverte pluridisciplinaire **HAL**, est destinée au dépôt et à la diffusion de documents scientifiques de niveau recherche, publiés ou non, émanant des établissements d'enseignement et de recherche français ou étrangers, des laboratoires publics ou privés.



Distributed under a Creative Commons Attribution - NonCommercial 4.0 International License

# Excellence in Chemistry Research

## Announcing our new flagship journal

- Gold Open Access
- Publishing charges waived
- Preprints welcome
- Edited by active scientists



## Meet the Editors of *ChemistryEurope*



**Luisa De Cola**

Università degli Studi  
di Milano Statale, Italy



**Ive Hermans**

University of  
Wisconsin-Madison, USA



**Ken Tanaka**

Tokyo Institute of  
Technology, Japan

# Role of Copper Migration in Nanoscale Ageing of Supported CuO/Al<sub>2</sub>O<sub>3</sub> in Redox Conditions: A Combined Multiscale X-ray and Electron Microscopy Study

Sharmin Sharna,<sup>[a, b]</sup> Virgile Rouchon,<sup>[a]</sup> Christèle Legens,<sup>[a]</sup> Anne-Lise Taleb,<sup>[a]</sup> Stefan Stanescu,<sup>[c]</sup> Corinne Bouillet,<sup>[b]</sup> Arnold Lambert,<sup>\*[a]</sup> Valerie Briois,<sup>[c]</sup> David Chiche,<sup>[a]</sup> Anne-Sophie Gay,<sup>[a]</sup> and Ovidiu Ersen<sup>[b]</sup>

Chemical Looping Combustion is a promising midterm solution to mitigate CO<sub>2</sub> emission, by carrying out indirect fuel combustion and allowing inherent separation of CO<sub>2</sub>. During the CLC process, an oxygen carrying material is subjected to successive oxidation-reduction reactions at high temperature which induce significant material degradation. CuO/Al<sub>2</sub>O<sub>3</sub> based materials have been widely considered as promising oxygen carriers (OC). However, the oxygen carrier ageing mechanisms (active phase migration and interactions with the support, phase transitions) are not well understood. Herein, an in-depth overview of the material evolution is achieved by employing a multi-scale characterization approach. At the  $\mu\text{m}$ -scale, copper

migration within the alumina support has been observed using Scanning Transmission X-ray Microscopy (STXM) and Scanning Electron Microscopy (SEM). The spatial distribution of the Cu–Al species provides information on copper mobility and the different phases interactions. A comprehensive mechanism is proposed concerning the redox behaviour of the CuO/Al<sub>2</sub>O<sub>3</sub> system, relating the diffusion of the Cu-species, the active phase-support interactions, and the role of copper in the Al<sub>2</sub>O<sub>3</sub> support phase transition to the temperature and the number of redox cycles. Understanding the ageing process of CuO/Al<sub>2</sub>O<sub>3</sub> materials paves a way to design more stable oxygen-carriers.

## Introduction

The rise of CO<sub>2</sub> levels in the atmosphere and the corresponding effect on the global climate demands for immediate actions in terms of reduction of CO<sub>2</sub> emissions.<sup>[1]</sup> A single solution is not enough to address this issue; therefore a range of solutions is proposed, including transition to lower carbon fuel, renewable energy, efficiency improvement of existing power plants, and CO<sub>2</sub> capture.<sup>[2]</sup> The implementation of CO<sub>2</sub> capture technology such as Chemical Looping Combustion (CLC) is an attractive approach due to the rising demand for fossil fuel as a


consequence of global population and economic growth.<sup>[3]</sup> CLC is a midterm solution for fossil fuel utilization with inherent carbon dioxide capture. The principle of CLC is to separate the combustion process in two steps: reduction and oxidation.<sup>[4]</sup> The process uses a metal-oxide based material termed as the oxygen carrier (OC). The OC is circulated in a “fuel reactor” where it provides oxygen to the fuel for indirect combustion. The OC material is either fully or partially reduced during this step. The by-products of the indirect combustion, which are CO<sub>2</sub> and H<sub>2</sub>O, are easily separated by condensation. A highly concentrated CO<sub>2</sub> stream is hence produced, ready for storage or utilization in other processes. The reduced OC is then regenerated, *i.e.* re-oxidized, by circulating through the “air reactor”. During the regeneration process, the (partially) reduced material reacts with air to re-form metal oxide. Thus, a full cycle of the reaction involves a redox reaction, typically above 800 °C. The advantage of the process lies in the separation of the oxidation and reduction steps, thus separating CO<sub>2</sub> gas from N<sub>2</sub> and residual O<sub>2</sub> stream which otherwise would require a post-combustion solution for separation. Therefore, CLC serves as a combustion process producing energy with the benefit of carbon dioxide separation, incurring low energy penalty.


In order for CLC to be economically feasible, special attention should be given to the development of the oxygen carrier which is at the core of the process.<sup>[5]</sup> Among the several types of materials proposed and studied, supported copper-based oxygen carriers received particular consideration due to their relatively low cost, acceptable environmental impact and flexible redox behavior making them ideal candidates for

[a] Dr. S. Sharna, Dr. V. Rouchon, Dr. C. Legens, A.-L. Taleb, Dr. A. Lambert, Dr. D. Chiche, Dr. A.-S. Gay  
IFP Energies nouvelles  
Rond-point de l'échangeur de Solaize  
BP3, 69360 Solaize (France)  
E-mail: arnold.lambert@ifpen.fr

[b] Dr. S. Sharna, Dr. C. Bouillet, Prof. O. Ersen  
Institut de Physique et de Chimie des Matériaux de Strasbourg  
67034 Strasbourg (France)

[c] Dr. S. Stanescu, Dr. V. Briois  
Synchrotron Soleil  
l'Orme des Merisiers  
BP48, 91192  
Saint-Aubin Gif-sur-Yvette (France)  
Homepage: www.synchrotron-soleil.fr

 Supporting information for this article is available on the WWW under <https://doi.org/10.1002/cctc.202201259>

 © 2023 IFP Energies nouvelles. ChemCatChem published by Wiley-VCH GmbH. This is an open access article under the terms of the Creative Commons Attribution Non-Commercial License, which permits use, distribution and reproduction in any medium, provided the original work is properly cited and is not used for commercial purposes.

industrial utilization.<sup>[6]</sup> In particular, CuO/Al<sub>2</sub>O<sub>3</sub> materials display promising outcome as a potential commercial oxygen carrier.<sup>[7–10]</sup>

Despite the suitability of CuO/Al<sub>2</sub>O<sub>3</sub> as an oxygen carrier, some drawbacks have been reported regarding the degradation of the material and loss of reactivity, especially at 900 °C or above.<sup>[7,11]</sup> Attrition, fragmentation and sintering of the copper oxides are identified as the main mechanisms resulting in the loss of reactivity. Attrition leads to a loss of copper phase due to the generation of copper-rich fines. After multiple redox cycles, oxygen carrier particles are subjected to fragmentation with the increase of support porosity.<sup>[11,12]</sup> While the copper-rich fines formed by attrition are related to the outward migration of the copper, the increased porosity in the particles is associated to the alumina phase transition.<sup>[7,13]</sup> Recently, Cabello et al. reported that the mechanical integrity of the OC is not affected when the redox cycling is carried out at 800 °C, compared to 900 °C or above.<sup>[14]</sup> This difference in the material behaviour could arise from multiple phase transformations during reactions, owing to high chemical and thermal stress during the redox cycles. Notably, CuO and Al<sub>2</sub>O<sub>3</sub> phases undergo solid state reaction at high temperature resulting in CuAl<sub>2</sub>O<sub>4</sub> formation.<sup>[10,13]</sup> Reportedly, the fresh OC composed of CuAl<sub>2</sub>O<sub>4</sub> (major phase), gamma alumina and traces of CuO, transforms to CuO (major phase), gamma alumina and traces of CuAl<sub>2</sub>O<sub>4</sub> after 10 h of redox cycling at 800 °C, and to mainly CuO and  $\alpha$ -Al<sub>2</sub>O<sub>3</sub> after 100 h of cycling.<sup>[9]</sup> The extent of  $\alpha$ -Al<sub>2</sub>O<sub>3</sub> formation is determined by reaction parameters such as temperature, number of cycles or OC conversion rate.<sup>[7,12,14]</sup> Regarding the various phase transitions and copper migration, Lambert et al. have suggested a comprehensive mechanism for the CuO-Al<sub>2</sub>O<sub>3</sub> system, subjected to long term redox cycling at 900 °C.<sup>[7]</sup> The authors proposed that the successive redox cycles result in the formation of large Cu<sup>0</sup> particles which may kinetically limit the re-formation of the copper aluminate phase. Consequently, the unreacted transition alumina would transform to  $\alpha$ -Al<sub>2</sub>O<sub>3</sub>. Finally, after *n* cycles, only  $\alpha$ -Al<sub>2</sub>O<sub>3</sub> phase and large crystallites of CuO would remain.<sup>[7]</sup> The proposed mechanism sheds light on the possible interactions in the CuO-Al<sub>2</sub>O<sub>3</sub> system which is crucial to determine the different phase transitions. However, it is limited to the phase transitions occurring at 900 °C and assumptions are made from a macroscopic perspective.

It is important to carry out a systematic study to understand the material's ageing by varying only the temperature and the number of cycles, keeping all the other reaction parameters constant. Furthermore, little is known regarding the stepwise evolution of the material as most of the studies report the bulk phases characterized by X-ray diffraction and the texture and copper repartition by Scanning Electron Microscopy (SEM), coupled eventually with Energy Dispersive X-ray Spectroscopy (EDS). However, information on the chemical nature of the phases cannot be achieved by SEM. The knowledge of the spatial distribution of the chemical elements and the polymorphic phases within the support can help understand the underlying mechanisms by which the evolution in the material occurs. It is crucial to make an association between the different

phases and how their transformation affects the overall composition, structural and morphological properties of the oxygen carrier and vice versa; in short, bridging the gap between the observed  $\mu$ m-scale properties and their relation to the nanoscale phenomena.

Herein, we report a study on the effect of temperature (700–900 °C) and the number of redox cycles (up to 200 cycles) on the evolution of CuO-Al<sub>2</sub>O<sub>3</sub> OC. A multi-scale understanding of the phases and the morphology was achieved by employing Scanning Transmission X-ray Microscopy (STXM) coupled with X-ray Absorption Near Edge Spectroscopy (XANES), and complemented by Scanning Electron Microscopy (SEM), Scanning Transmission Electron Microscopy (STEM), X-ray diffraction (XRD) and hard X-ray Absorption Spectroscopy (XAS) analyses.

## Results and Discussion

### Reference XANES spectra of the Copper-Alumina phases

#### Cu L-edge Spectra

The Cu L<sub>2,3</sub>-edge absorption spectra of the reference phases CuO, CuAl<sub>2</sub>O<sub>4</sub> and Cu<sup>0</sup> are displayed in Figure 1. The main peak for metallic copper is at 936.5 eV which is attributed to the 2p→4s transition as well some contribution from 3d–4s hybridization.<sup>[15]</sup> The CuO phase where Cu is in the +2 oxidation state can be identified by the two main peaks at ~934.2 eV and ~954 eV assigned to transitions of the Cu 2p<sub>3/2</sub> (L<sub>3</sub>) and 2p<sub>1/2</sub> (L<sub>2</sub>) electrons into empty d-states, respectively. The characteristic features of CuO include the broad peak at ~941.5 eV and a separation of about 19.8 eV between the L<sub>3</sub> and L<sub>2</sub> peaks (the spin-orbit coupling).<sup>[16]</sup> For the CuAl<sub>2</sub>O<sub>4</sub> reference sample, the L<sub>3</sub> and L<sub>2</sub> main transitions are located at 932.9 eV and ~953 eV, respectively. CuAl<sub>2</sub>O<sub>4</sub> is a spinel-like structure that contains both tetrahedral CuO<sub>4</sub> and octahedral CuO<sub>6</sub> species. Therefore, the L<sub>3</sub> peak displays a shoulder at ~933.6 eV which is assigned to the CuO<sub>6</sub> species.<sup>[17]</sup> The difference in the bonding environments (square planar in CuO and tetrahedral and octahedral configurations in CuAl<sub>2</sub>O<sub>4</sub>) leads to the subtle changes in the energies.<sup>[18]</sup>

The spectral features (number of peaks, distance between the peaks and the energy difference between two species) remain similar compared to the literature.<sup>[19]</sup> Here, the spectra display a shift of a few eV, possibly resulting from the calibration of the monochromator. However, spectral resemblance is more important to identify the different species present. The energy difference between the L<sub>3</sub> peaks of CuAl<sub>2</sub>O<sub>4</sub> and CuO is about ~1.3 eV. The energy difference between the tetrahedral and the octahedral sites in CuAl<sub>2</sub>O<sub>4</sub> is about 0.7 eV. Thus, the sensitivity of the XANES allows to distinguish the corresponding components as well as Cu-coordination.

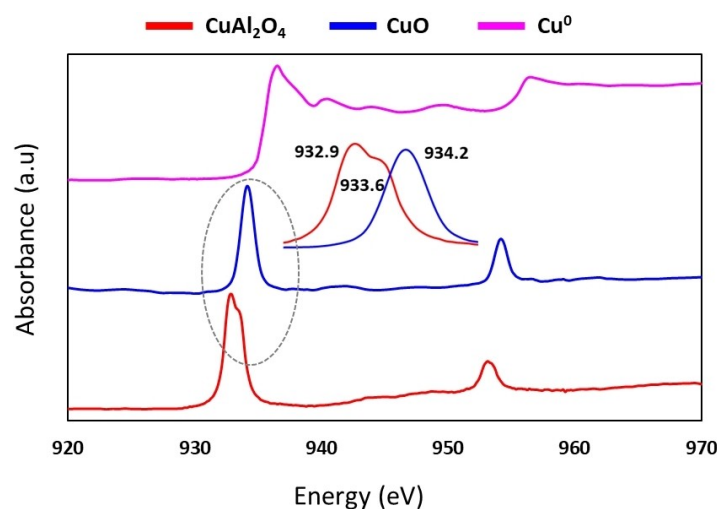


Figure 1. Reference spectra of CuO, CuAl<sub>2</sub>O<sub>4</sub> and Cu<sup>0</sup> phases at Cu L-edge.

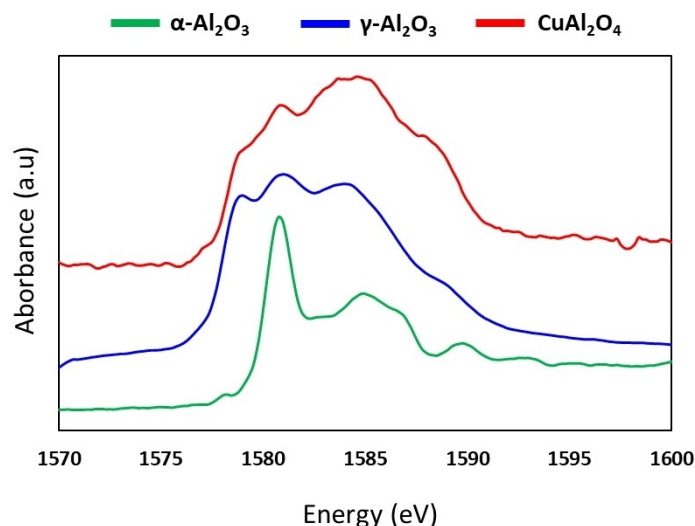


Figure 2. Reference spectra of CuAl<sub>2</sub>O<sub>4</sub>, γ-Al<sub>2</sub>O<sub>3</sub> and α-Al<sub>2</sub>O<sub>3</sub> phases at Al K-edge.

### Al K-edge Spectra

For the Al-containing references, three distinct peaks are observed at the Al K edge corresponding to the tetrahedral or Td (AlO<sub>4</sub>) and octahedral or Oh (AlO<sub>6</sub>) coordination environments.<sup>[20,21]</sup> Depending on the proportion of the coordination sites, the relative peak intensities change. Therefore, the different Al-containing samples can be identified from the site-occupancy dependent peak intensities as shown for the Al-containing reference samples in Figure 2. The assignment of the peaks and the corresponding transitions are summarized in Table S.2.

The α-Al<sub>2</sub>O<sub>3</sub> phase only contains Al octahedrally coordinated with 6 oxygen atoms, displaying two prominent peaks at 1580.8 and 1584.9 eV.<sup>[22]</sup>

The γ-Al<sub>2</sub>O<sub>3</sub> phase is typically considered to have a spinel-type structure composed of octahedral and tetrahedral Al<sup>3+</sup> coordination sites.<sup>[23]</sup> The first peak at 1579 eV displays the contribution from the tetrahedral occupancy. The peaks at 1581.0 and 1584.0 eV are assigned to similar transitions as those of α-Al<sub>2</sub>O<sub>3</sub> arising from the octahedral environment.<sup>[22]</sup>

For the CuAl<sub>2</sub>O<sub>4</sub> sample, the peak assignments are similar to those of γ-Al<sub>2</sub>O<sub>3</sub> transition phases since both γ-Al<sub>2</sub>O<sub>3</sub> and CuAl<sub>2</sub>O<sub>4</sub> are spinel-type structures. The proportions of Al with octahedral vs tetrahedral coordination change since the spinel structure accommodates Cu<sup>2+</sup> ions as well.<sup>[24]</sup> With regards to the AlO<sub>4</sub>:AlO<sub>6</sub> species ratio, in CuAl<sub>2</sub>O<sub>4</sub> there is less Al atoms in Td sites compared to γ or θ-Al<sub>2</sub>O<sub>3</sub>.

Our reference spectra are in good agreement with the XANES features of different alumina polymorphs and CuAl<sub>2</sub>O<sub>4</sub> reported in the literature.<sup>[20]</sup>



It is speculated that the sample may contain other transition aluminas such as  $\delta$ - $\text{Al}_2\text{O}_3$  and  $\theta$ - $\text{Al}_2\text{O}_3$  resulting from the polymorphic phase transition of  $\gamma$ - $\text{Al}_2\text{O}_3$  phase to  $\delta$ - $\text{Al}_2\text{O}_3$  and eventually to  $\theta$ - $\text{Al}_2\text{O}_3$ . The phase transition leads to increase in the occupancy of the tetrahedral sites by the  $\text{Al}^{3+}$  cation. The peak corresponding to the  $\text{AlO}_4$  species, at  $\sim 1579$  eV would display higher relative intensity as a function of the phase transition progress according to the experimental observation of Kato et al.<sup>[20]</sup>

## Fresh oxygen carriers

### Phase information

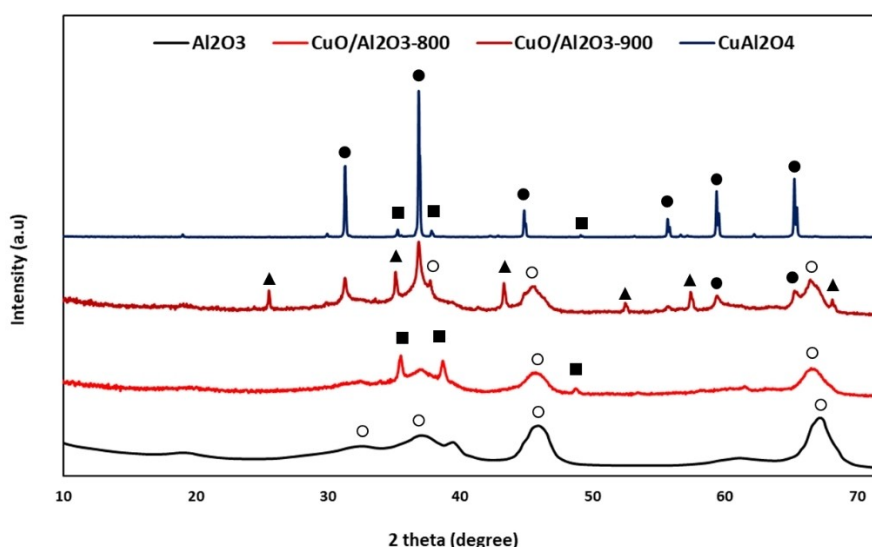
Figure 3 displays the diffractograms of the support composed of  $\gamma$ - $\text{Al}_2\text{O}_3$ , and of  $\text{CuO}/\text{Al}_2\text{O}_3$ -800,  $\text{CuO}/\text{Al}_2\text{O}_3$ -900 and  $\text{CuAl}_2\text{O}_4$ . After impregnation, the fresh oxygen carriers calcined at 700 (not shown here) and 800 °C contain a mixture of CuO, copper aluminate and possibly some transition aluminas, whereas calcination at 900 °C leads to a mixture of copper aluminate,  $\alpha$ - $\text{Al}_2\text{O}_3$  and transition aluminas.

Following the impregnation of the support with copper nitrate salt, the first step involves thermal decomposition of  $\text{Cu}(\text{NO}_3)_2$  to CuO, which may eventually undergo solid-state reaction with  $\gamma$ - $\text{Al}_2\text{O}_3$  to form copper aluminate,  $\text{CuO} + \text{Al}_2\text{O}_3 \rightarrow \text{CuAl}_2\text{O}_4$ . Additionally, alumina phase transition may also take place as a function of the calcination temperature.

The diffractograms display significant differences in the copper aluminate features, for example the peak corresponding to copper aluminate/transition alumina in  $\text{CuO}/\text{Al}_2\text{O}_3$ -800 sample are much broader, exhibiting similar features as the initial  $\gamma$ - $\text{Al}_2\text{O}_3$  phase. The formation of cubic mixed-spinel  $\text{CuAl}_2\text{O}_4$  results from the occupation of  $\text{Cu}^{2+}$  cations in the available octahedral and tetrahedral positions in the structure of  $\gamma$ - $\text{Al}_2\text{O}_3$ , which is a defective spinel.<sup>[20,25]</sup> Since, both  $\gamma$ - $\text{Al}_2\text{O}_3$

and  $\text{CuAl}_2\text{O}_4$  are cubic spinel, they have similar diffraction patterns. A slight difference comes from the shift of the  $\text{CuAl}_2\text{O}_4$  peaks towards lower  $2\theta$  angles due to an increase in the lattice parameter following the insertion of  $\text{Cu}^{2+}$  ions. As the oxygen carrier contains 13 wt % of CuO (i.e. a maximum of 10.4 wt % of Cu), compared to 35 wt % of Cu in stoichiometric  $\text{CuAl}_2\text{O}_4$ , the chemical-structural representation of the Cu-Al-O system may take various chemical forms of the spinel structure. Two extreme cases can be represented by (1) homogeneous non-stoichiometric copper aluminate ( $\text{NS-Cu}_x\text{Al}_y\text{O}_4$ ) and (2) an intricate mixture of x% of  $\text{CuAl}_2\text{O}_4$  with y% of  $\text{Al}_2\text{O}_3$ . We emphasize that both possibilities do exist and that a proper representation of the system is through a solid solution in between the  $\text{CuAl}_2\text{O}_4$  and  $\gamma$ - $\text{Al}_2\text{O}_3$  end-members, encompassing the compositional range of the  $\text{Cu}_x\text{Al}_y\text{O}_4$  structural formula. Therefore, to simplify the description it is assumed that the sample is composed of non-stoichiometric copper aluminate ( $\text{Cu}_x\text{Al}_y\text{O}_4$ ). This assumption is made based on the XANES of the  $\text{CuO}/\text{Al}_2\text{O}_3$ -800 which displays similar features as  $\text{CuAl}_2\text{O}_4$  at both Cu L-edges and Al K-edge, meanwhile the TEM-EDS indicates 8–10 wt % of copper throughout the interior of the sample. It should be noted that the stoichiometry of the copper aluminate phase may vary within the grain, which is especially true for the  $\text{CuO}/\text{Al}_2\text{O}_3$ -900 which displays sharp peaks corresponding to  $\text{CuAl}_2\text{O}_4$  as well as broader peaks similar to the  $\text{CuO}/\text{Al}_2\text{O}_3$ -800 sample. Therefore a precise sub-stoichiometric formula could not be proposed as, depending on the amount of copper incorporated in the sample which varies at different length scales,  $\text{Cu}^{2+}$  vacancies may be compensated either by  $\text{Al}^{3+}$  ions replacing  $\text{Cu}^{2+}$  positions or  $\text{O}^{2-}$  vacancies to compensate for the charge distributions.<sup>[26,27]</sup>

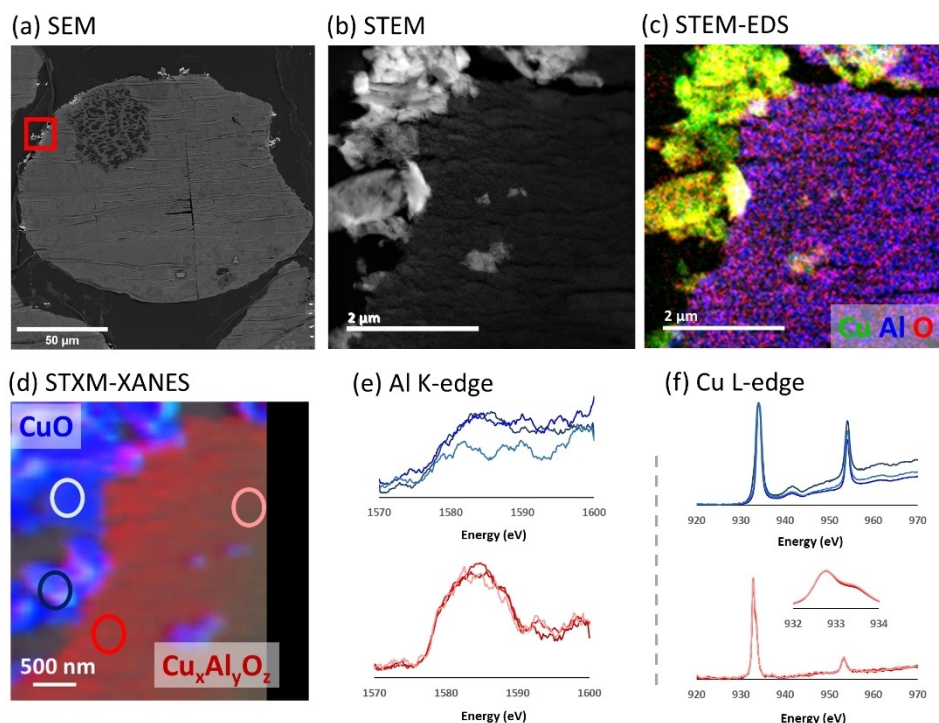
Moreover, the presence of non-stoichiometric copper aluminate can also be deduced from the *in situ* XRD data during the stepwise calcination of the  $\text{CuO}/\text{Al}_2\text{O}_3$ -800 from 800 to 900 °C (presented in SI.4.1). A loss of CuO peaks and simultaneous shift



**Figure 3.** XRD patterns of  $\text{Al}_2\text{O}_3$ ,  $\text{CuO}/\text{Al}_2\text{O}_3$  samples calcined at 800 and 900 °C and  $\text{CuAl}_2\text{O}_4$  with CuO (■),  $\text{CuAl}_2\text{O}_4$  (●),  $\gamma$ - $\text{Al}_2\text{O}_3$  (○), and  $\alpha$ - $\text{Al}_2\text{O}_3$  (▲).

**Table 1.** Identification of copper and alumina phases in the calcined sample from XRD and quantification of Cu species (% relative spectrum) by XAS (the LCF of the spectra are provided in SI.2.1).

	Al <sub>2</sub> O <sub>3</sub>	CuO/Al <sub>2</sub> O <sub>3</sub> -700 °C	CuO/Al <sub>2</sub> O <sub>3</sub> -800 °C	CuO/Al <sub>2</sub> O <sub>3</sub> -900 °C
XRD	γ-Al <sub>2</sub> O <sub>3</sub>	CuO, Cu <sub>x</sub> Al <sub>y</sub> O <sub>4</sub> , transition alumina	CuO, Cu <sub>x</sub> Al <sub>y</sub> O <sub>4</sub> , transition alumina	Cu <sub>x</sub> Al <sub>y</sub> O <sub>4</sub> , transition alumina, α-Al <sub>2</sub> O <sub>3</sub>
XAS Cu K-edge	–	CuO:Cu <sub>x</sub> Al <sub>y</sub> O <sub>4</sub> = 45:55	CuO:Cu <sub>x</sub> Al <sub>y</sub> O <sub>4</sub> = 30:70	Cu <sub>x</sub> Al <sub>y</sub> O <sub>4</sub>

**Figure 4.** Fresh CuO/Al<sub>2</sub>O<sub>3</sub>-800 sample: (a) SEM, (b) STEM, (c) STEM-EDS depicting the repartition of Cu and Al contents respectively, and overlay of Cu, Al and O contents and (d) STXM-XANES with contribution of copper aluminate and CuO as the colored map of the two phases and the spectral features at (e) Al K-edge and (f) Cu L-edges corresponding to the colored circles marked on image (d).

of the alumina peaks is evident from the data, implying possible insertion of the Cu<sup>2+</sup> ion.

The assumption of Cu<sub>x</sub>Al<sub>y</sub>O<sub>4</sub> is in agreement with Shimizu *et al.* where the authors display differences in XRD peaks position and broadening of the copper-aluminate as well as difference in XAS features depending on the amount of copper in the copper aluminate.<sup>[17]</sup>

In addition to XRD, XAS at Cu K-edge provides an average of the compositions present in the samples calcined at 700, 800 and 900 °C. From linear combination fitting of the XANES domain, the proportions of CuO and Cu<sub>x</sub>Al<sub>y</sub>O<sub>4</sub> spectra are found. As presented in Table 1, the amount of Cu<sub>x</sub>Al<sub>y</sub>O<sub>4</sub> increases with the calcination temperature. In the CuO/Al<sub>2</sub>O<sub>3</sub>-900 sample, no CuO feature is found and the sample is composed of NS copper aluminate in terms of the copper phase.

### Morphological information

Figure 4 displays the cross-section SEM image (a) of the whole grain of the CuO/Al<sub>2</sub>O<sub>3</sub>-800 sample, as well as the dark-field STEM image (b), the corresponding Cu–Al–O EDS map (c) and

STXM map (d) of the red squared region highlighted on the SEM image. From the SEM, three main features are identified: large copper-rich crystallites at the periphery of the grains, probably due to a slight excess of solution volume during incipient wetness impregnation, Cu-concentration gradient from the edge (slightly higher) to the interior of the grain and a homogeneous distribution of copper inside the grain.

The extracted spectra at Cu L-edges from the different regions of the STXM map show the presence of CuO (in dark and light blue circles) with the L<sub>3</sub> peak at 934 eV and Cu<sub>x</sub>Al<sub>y</sub>O<sub>4</sub> (in red and pink circles) at 933 eV. At Al K-edge, the blue spectra show absorption corresponding to the different alumina/aluminate phases, but the local concentration in Al is too low to achieve proper assignment of the spectra to any phase. In the local region of the aluminate matrix (Figure 3, identified in red), the reference spectra of the γ-Al<sub>2</sub>O<sub>3</sub> and Cu-aluminate phases were used as components to compute the respective spectral contribution in the energy stacks of the different regions of interest (ROI) using Singular Value Decomposition (SVD) analysis. No contribution from the γ-Al<sub>2</sub>O<sub>3</sub> could be identified. Hence, it can be concluded that the Al K-edge signal is solely coming from the Cu-aluminate phase and any discrepancies arising

from one area to another is linked to the different proportions of copper within the alumina structure, as mentioned before.

The average percentage of copper inside the grain was estimated to be around 8–10 wt% from the TEM-EDS, equivalent to the impregnated percentage of copper. The STEM image (Figure 4b) displays variations in the greyscale implying a copper concentration gradient from higher percentage at the edge of the grain to lower percentage away from the edge. The interior of the grain appears to be homogeneous as presented in SI.5.1.

The fresh  $\text{CuO}/\text{Al}_2\text{O}_3$ -900 sample displays a heterogeneous morphology with three main features shown in Figure 5: the interior of the grain appears to be less porous with relatively uniform greyscale and the edge of the grain is composed of either higher or lower porosity areas presenting a darker and lighter contrast, respectively. Parallel wavy lines across the grains in the SEM image are preparation artefacts resulting from ultramicrotomy sectioning.

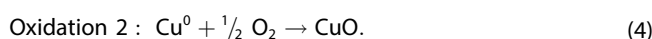
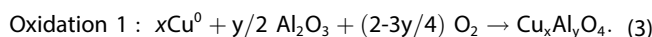
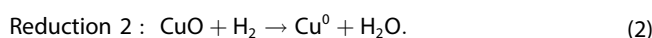
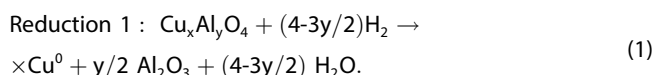
From the higher resolution STEM-EDS analysis, the interior of the grain contains an average of 8–10 wt% Cu. The lighter-contrasted regions of the grain edge are rich in Cu, presenting 15 to 30 wt% of copper. The dark contrasted areas are more porous and devoid of copper, mainly composed of large alumina particles. From the well-resolved spectral features gained from XANES, the phases corresponding to the different morphologies and copper concentrations could be identified. The STXM map at the edge of the grain depicts alpha alumina phase (marked in green) in the areas with higher porosity and coarser particles, containing no copper and darker contrast in

the SEM/STEM image (Figure 5). The denser area with lighter contrast and higher proportions of copper is identified as Cu-aluminate phase (in red). Similar to the  $\text{CuO}/\text{Al}_2\text{O}_3$ -800, the interior of the grain appears to be homogeneous as presented in SI.5.2.

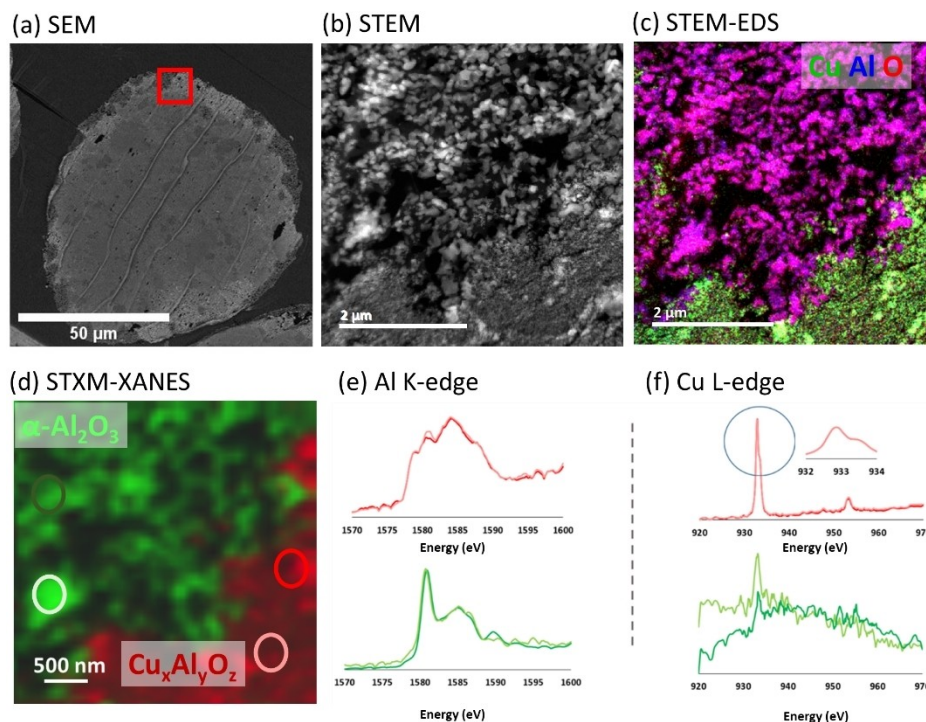
The correlation between STEM/SEM grey scales and STXM phase assignment allows for a comprehensive interpretation of the grey scales to be systematically applied to all STEM and SEM images.

## Redox cycles at 900 °C

The redox cycles involve the following reactions:



During the reduction steps, metallic copper is formed from the reduction of copper aluminate (Reduction 1) or copper oxide (Reduction 2). In the subsequent re-oxidation step, the oxide phases will be recovered via Oxidation 1 and Oxidation 2. The  $\text{Al}_2\text{O}_3$  support devoid of any copper after the reduction

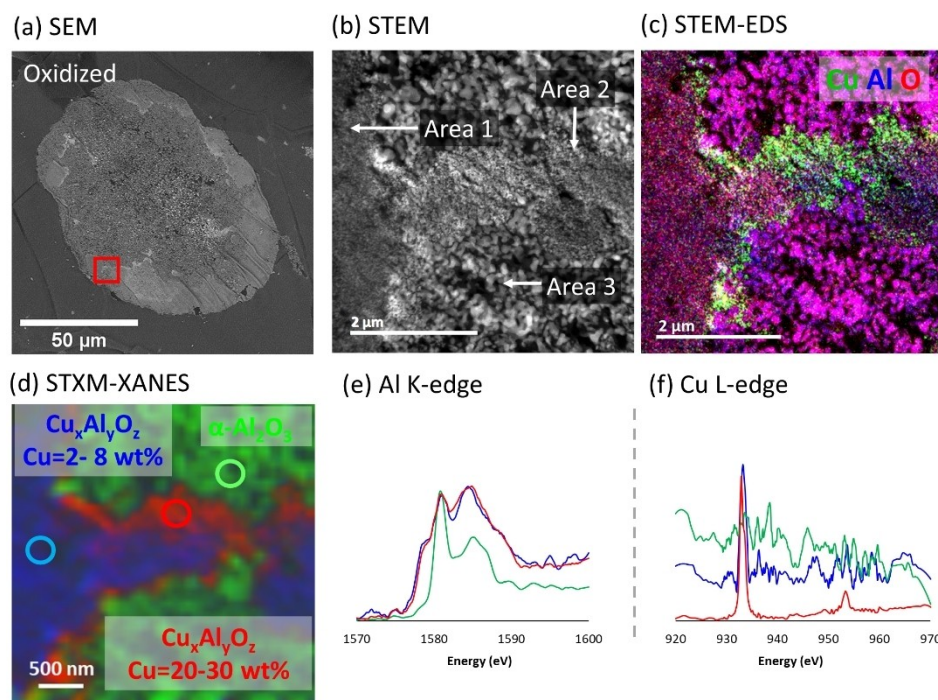


**Figure 5.** Fresh  $\text{CuO}/\text{Al}_2\text{O}_3$ -900 sample: (a) SEM, (b) STEM, (c) STEM-EDS depicting the repartition of Cu and Al contents respectively, and overlay of Cu, Al and O contents and (d) STXM-XANES with contribution of  $\alpha$ - $\text{Al}_2\text{O}_3$  and copper aluminate as colored map and the spectral features at (e) Al K-edge and (f) Cu L-edges corresponding to the colored circles marked on image d.



**Table 2.** Identification of the copper and alumina phases in the CuO/Al<sub>2</sub>O<sub>3</sub>-900 samples after 50 and 200 cycles at 900 °C from XRD (diffractograms presented in SI.3.1) and quantification of Cu species (% relative spectrum) by Cu K-edge XAS (spectral fitting provided in SI.2.2).

	CuO/Al <sub>2</sub> O <sub>3</sub> -900-50 cycles	CuO/Al <sub>2</sub> O <sub>3</sub> -900-200 cycles
XRD	CuO (major), Cu <sub>x</sub> Al <sub>y</sub> O <sub>4</sub> , α-Al <sub>2</sub> O <sub>3</sub>	CuO (major), α-Al <sub>2</sub> O <sub>3</sub> (major), Cu <sub>x</sub> Al <sub>y</sub> O <sub>4</sub> (trace)
XAS, CuO:Cu <sub>x</sub> Al <sub>y</sub> O <sub>4</sub>	75:25	90:10

**Figure 6.** CuO/Al<sub>2</sub>O<sub>3</sub>-900 sample, after 50 cycles in oxidized state: (a) SEM, (b) STEM, (c) STEM-EDS depicting the repartition of Cu and Al contents respectively, and overlay of Cu, Al and O contents and (d) STXM-XANES colored map with contribution of α-Al<sub>2</sub>O<sub>3</sub> and copper aluminate with different Cu-concentration and the spectral features at (e) Al K-edge and (f) Cu L-edges corresponding to the colored circles marked on image d.

steps will be referred to as Cu-less aluminate. It is believed that this reduction product of Cu-aluminate does not exactly resemble any of the transition aluminas as the structure undergoes vacancy formation and filling at every successive reduction and oxidation. Therefore, this phase is likely to have structural defects incurred during the long-term redox cycling. The fate of this phase is discussed in detail later in the article.

The characterization of the CuO/Al<sub>2</sub>O<sub>3</sub>-900 series after 50 and 200 cycles is highlighted first. The redox reactions were carried out at 900 °C, corresponding to the temperature of calcination. This set of samples has been characterized thoroughly employing both the phase and morphological characterizations. Later, the effect of lower cycling temperature will be discussed.

In Table 2, the overall phase distribution calculated from XRD data and CuO:Cu<sub>x</sub>Al<sub>y</sub>O<sub>4</sub> ratio (XAS at the Cu K edge) are summarized for the sample after 50 and 200 cycles in their oxidized form. After 50 cycles, CuO represents the majority of the copper-containing phase. A small proportion of copper aluminate is also present together with α-Al<sub>2</sub>O<sub>3</sub> phase. Subsequently, α-Al<sub>2</sub>O<sub>3</sub> makes up the majority of the support grain in the sample after 200 cycles, in which copper mainly exists as

CuO and only trace amount of copper aluminate is noted. From XAS, the ratio of CuO:Cu<sub>x</sub>Al<sub>y</sub>O<sub>4</sub> is found to be 75:25 and 90:10 in the samples after 50 and 200 cycles, respectively.

### 50 cycles-oxidized sample

The evolution of the sample after 50 cycles is displayed in Figure 6 in oxidized form. As observed from the STEM-EDS and STXM maps in Figure 6, the oxidized sample exhibits three different morphologies associated to different amounts of copper. Area 1 contains a dense support matrix with a low concentration of copper (about 2–8 wt%). Area 2 contains a higher concentration of Cu (20–30 wt%) and lies in between area 1 and area 3. In area 2, some porosity is observed, and the individual particles are larger compared to area 1. Both areas 1 and 2 are made of Cu<sub>x</sub>Al<sub>y</sub>O<sub>4</sub> with different proportions of copper. Area 3 is made of large Al-rich particles forming a porous network. These Al-rich particles do not contain any copper, and from the particles morphology they can be assigned to alpha alumina. The size of these particles is in the range of above 100 nm in length and 100 to 200 nm in width.

Within the  $\alpha$ - $\text{Al}_2\text{O}_3$  matrix, large CuO particles have also been found, depicting a wide size range of 50 to 500 nm. The spatial distribution of  $\text{Cu}_x\text{Al}_y\text{O}_4$  with low and high copper concentration and the  $\alpha$ - $\text{Al}_2\text{O}_3$  display a copper concentration gradient and a sharp textural front, likely related to a correlated phase transition and Cu-migration front.

### 50 cycles – reduced sample

As observed from the SEM image in Figure 7, the grain seems to be composed of a mixture of higher porosity zones containing  $\alpha$ - $\text{Al}_2\text{O}_3$  and denser areas made of Cu-less aluminate matrix. Between these two regions, copper particles (between 50 nm to a few  $\mu\text{m}$  in size) are found scattered within the

porosity of the front region between  $\alpha$ - $\text{Al}_2\text{O}_3$  and Cu-less aluminate matrix. Some copper particles are also found in the denser matrix with a smaller size range, and in the alpha domain matrix with larger size range. The chemical speciation, obtained by STXM, of the reduced sample is shown in Figure 7. In the characterized area, only the presence of metallic copper (red) and  $\alpha$ - $\text{Al}_2\text{O}_3$  (green) is noted.

### 200 cycles-Oxidized sample

From the SEM image in Figure 8, after 200 cycles, the sample is mainly composed of large crystallites of CuO and alpha alumina phase. The increased porosity in the alumina support is visible. The alpha alumina particles are larger than 500 nm. The size of

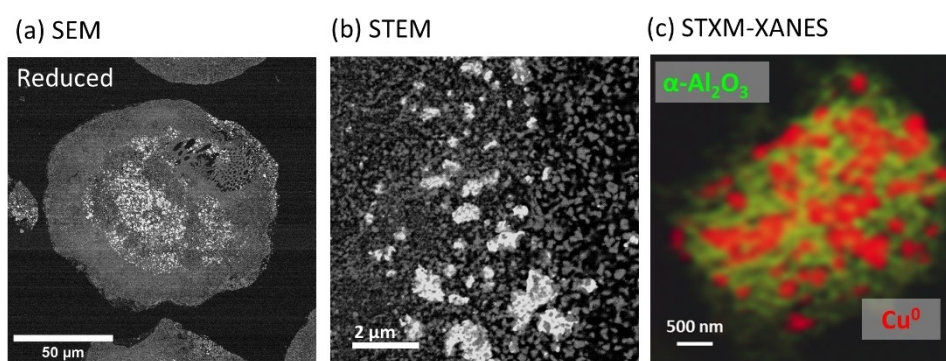


**Figure 7.** (a) SEM, (b) STEM and (c) STXM-XANES images acquired in different areas on the reduced samples after 50 cycles.

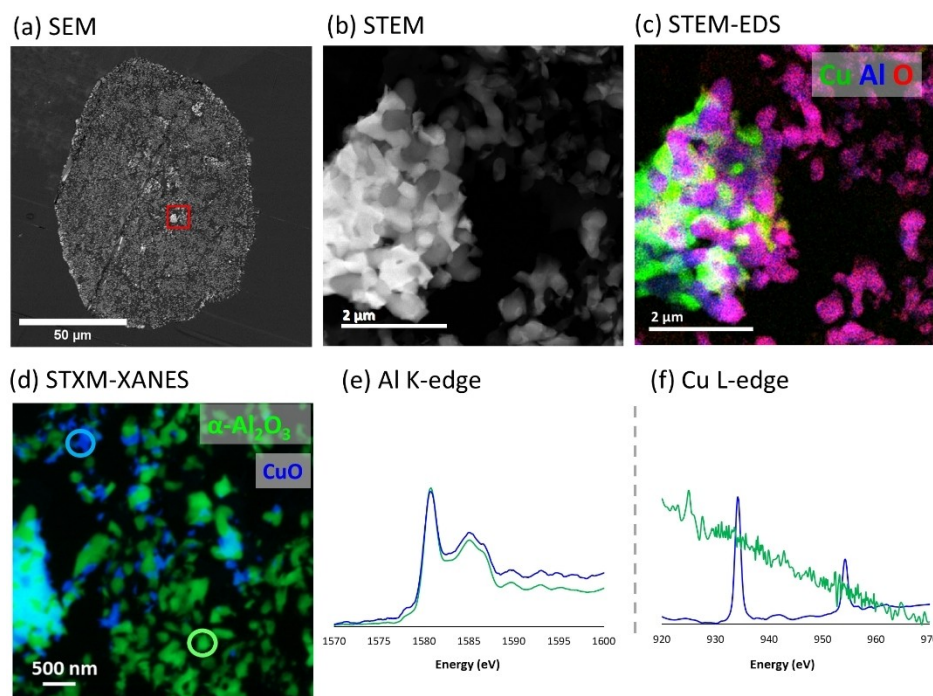


**Figure 8.** CuO/ $\text{Al}_2\text{O}_3$ -900 sample, after 200 cycles in oxidized state: (a) SEM, (b) STEM, (c) STEM-EDS depicting the repartition of Cu and Al contents respectively, and overlay of Cu, Al and O contents and (d) STXM-XANES colored map with contribution of  $\alpha$ - $\text{Al}_2\text{O}_3$  and CuO and the spectral features at (e) Al K-edge and (f) Cu L-edges corresponding to the colored circles marked on image d.

the copper oxide particles is above 200 nm. CuO particles also exhibit irregular shapes, mostly molding into the alumina macropores, where the white particles (CuO) are observed to be encompassing the grey particles ( $\alpha$ -Al<sub>2</sub>O<sub>3</sub>). The chemical speciation from the STXM-XANES analysis displays the two dominant phases identified by XRD.

### Phase transition, interaction with Al<sub>2</sub>O<sub>3</sub> support and copper migration

The overall evolution of the oxygen carrier is summarized in Figure 9, redox cycling at 900 °C leads to drastic changes in the material in terms of phase distribution, particle size and porosity. From an initial mesoporous copper aluminate sample with various local proportions of copper, the OC transforms into highly macroporous  $\alpha$ -Al<sub>2</sub>O<sub>3</sub> with large CuO crystallites. The OC undergoing 50 cycles displays an intermediate state containing copper aluminate (with different concentrations),  $\alpha$ -Al<sub>2</sub>O<sub>3</sub> and CuO. Moreover, there exists a copper concentration gradient at the frontier between the macroporous  $\alpha$ -Al<sub>2</sub>O<sub>3</sub> zones and Cu-aluminate zones as demonstrated from the oxidized and reduced samples after 50 cycles. The final oxidized state of the OC after 200 cycles corresponds to a complete chemical segregation of Cu and Al between CuO and  $\alpha$ -Al<sub>2</sub>O<sub>3</sub> phases.

### Formation of Copper phases

The gradual phase transition to alpha alumina has an impact on the other phases, such as the relative phase proportions of Cu<sub>x</sub>Al<sub>y</sub>O<sub>4</sub> and CuO. Initially, Cu<sub>x</sub>Al<sub>y</sub>O<sub>4</sub> is formed via solid state reaction between CuO and  $\gamma$ -alumina. During reduction, Cu<sub>x</sub>Al<sub>y</sub>O<sub>4</sub> forms metallic copper. As observed in the reduced sample after 50 cycles, the copper phase migrates through the porous  $\alpha$ -Al<sub>2</sub>O<sub>3</sub> and the Cu-less region and forms large particles

surrounding the matrix grains. During the following oxidation, the large Cu particles at the phase front are locally redispersed back to the Cu-deficient aluminate to re-form Cu<sub>x</sub>Al<sub>y</sub>O<sub>4</sub>, while the Cu particles in the microporous  $\alpha$ -Al<sub>2</sub>O<sub>3</sub> are oxidized to CuO and retaining their relative dispersion because of their incapacity to form an aluminate with  $\alpha$ -Al<sub>2</sub>O<sub>3</sub> at such temperatures. Indeed, the reaction between CuO and  $\alpha$ -Al<sub>2</sub>O<sub>3</sub> requires either higher temperature or longer reaction duration as reported by Hu et al.<sup>[28]</sup> Hence, in the reaction conditions of the current study, the gradual formation of the alpha phase leads to accumulation of the CuO phase at the expense of the copper aluminate. Eventually, the accumulation of CuO promotes its particle size increase as a function of the number of cycles.

### Formation of $\alpha$ -Al<sub>2</sub>O<sub>3</sub>

Alpha alumina is thermodynamically the most stable form of the Al<sub>2</sub>O<sub>3</sub> family. It should be noted that typically, the formation of the alpha phase occurs at a temperature above 1000 °C, without the presence of any other metallic element. In the current study, the alpha alumina phase transition occurs at temperatures as low as 700 °C (described in a later section). This leads to the conclusion that the presence of copper promotes the alpha alumina transition by lowering the phase transition temperature, in agreement with previous studies.<sup>[24,29]</sup> Nevertheless, the phase transition temperature of alumina is also affected by other factors such as surface properties, alumina particles size and presence of water, among others.<sup>[30]</sup> Hence, a control experiment was carried out with the pure  $\gamma$ -Al<sub>2</sub>O<sub>3</sub> support. To ensure fair comparison, a similar protocol of incipient wetness impregnation (with water only) was performed on the  $\gamma$ -Al<sub>2</sub>O<sub>3</sub> support. After drying and calcination, the water-impregnated alumina support was subjected to 50 redox cycles at 900 °C, which is equivalent to 20 hours of thermal treatment. No  $\alpha$ -Al<sub>2</sub>O<sub>3</sub> has been found from the XRD of the

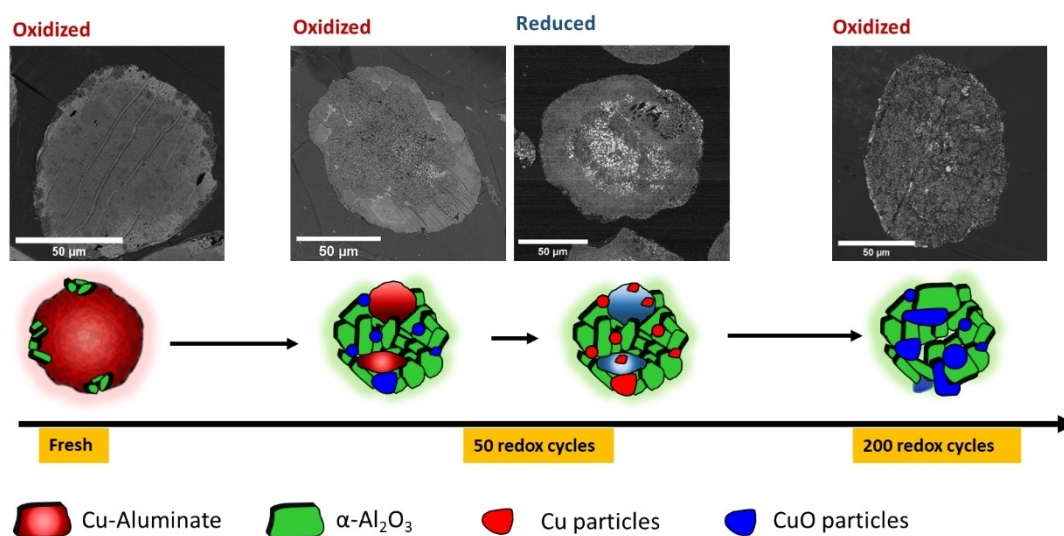


**Figure 9.** Schematic representation of the redox cycle dependent changes in the oxygen carrier at 900 °C.



water-impregnated sample, confirming that the presence of copper lowers the phase transition temperature to the alpha phase.

Pure  $\gamma\text{-Al}_2\text{O}_3$  to  $\alpha\text{-Al}_2\text{O}_3$  transformation follows a transition sequence of  $\gamma \rightarrow \delta \rightarrow \theta \rightarrow \alpha\text{-Al}_2\text{O}_3$ .<sup>[25]</sup> If we consider the structural configurations of the different aluminas, the transition aluminas are composed of Face-Centered Cubic (FCC) arrangement with different proportions of  $\text{AlO}_4$  and  $\text{AlO}_6$ , whereas the alpha phase is made of  $\text{AlO}_6$  arranged in Hexagonal Close-Packed (HCP). In this sequence the percentage of the  $\text{Al}^{3+}$  ions in the tetrahedral configuration increases from the  $\gamma$ -phase (~40:60) to  $\delta$  to the  $\theta$ -phase, reaching a  $\text{AlO}_4:\text{AlO}_6$  ratio of 50:50. Since the alpha phase is only composed of  $\text{AlO}_6$  environments, the  $\theta$  to  $\alpha$  transition would involve movement of the  $\text{Al}^{3+}$  sites which requires high activation energy.<sup>[28]</sup> Additionally, the oxygen position has to be reconfigured from an FCC structure in the  $\theta$ -phase to HCP arrangement in the  $\alpha$ -phase. Hence, the overall phase alpha transition is energy-intensive requiring an estimated activation energy of 605 kJ/mol via the transition aluminas pathway.<sup>[29]</sup> In contrast, the activation energy is reported to be of 510 kJ/mol for the copper-promoted (impregnation of  $\gamma\text{-Al}_2\text{O}_3$  with 8 wt% CuO) alpha-alumina transition.<sup>[29]</sup> Therefore, it can be deduced that the presence of copper lowers the overall phase transition energy barrier. The exact role of copper is debated, with some studies suggesting the  $\text{CuAl}_2\text{O}_4$  phase acts as a heterogenous nucleation site, while other studies report the presence of a "Cu-modified" alumina structure, before the emergence of  $\alpha\text{-Al}_2\text{O}_3$ .<sup>[22,26,27]</sup> In this study, we propose a pathway based on the modification of the Al–O bonding environment. Figure 10 displays the Al K-edge spectra of reference  $\gamma\text{-Al}_2\text{O}_3$ , reference  $\text{CuAl}_2\text{O}_4$ , fresh oxygen carrier calcined at 900 °C (taken from the area containing Cu-aluminate) and the sample cycled after 50 times (taken from the area containing low Cu-content Cu-aluminate). The peak at 1579 eV corresponds to tetrahedral  $\text{AlO}_4$  and the peaks at 1581 and 1584 eV are associated to the octahedral sites. From the ratio of peak areas at 1579 and 1581 eV it is possible to quantify

the relative proportion of the two environments.<sup>[16]</sup> The different intensities at the two peaks for  $\gamma\text{-Al}_2\text{O}_3$  and  $\text{CuAl}_2\text{O}_4$  phases is evident from the graph displayed in Figure 10. The area of the two peaks were estimated by curve fitting analysis using pseudo-Voigt function. The  $\text{AlO}_4:\text{AlO}_6$  ratio is found to be 40:60 and 30:70 for the reference  $\gamma\text{-Al}_2\text{O}_3$  and  $\text{CuAl}_2\text{O}_4$  materials. From this difference, it can be deduced that the  $\text{Cu}^{2+}$  ions insertion in the alumina leads to the diffusion of some  $\text{Al}^{3+}$  ions from tetrahedral to octahedral sites. Furthermore, after 50 cycles, the tetrahedral to octahedral ratio is approximately 20:80. With the progression of the number of redox cycles, the relative proportions of the  $\text{AlO}_6$  seem to increase which may indicate a slow progression towards the alpha phase transition. Presumably, changes in the Al–O bonding environment in the  $\text{Cu}_x\text{Al}_y\text{O}_4$  phase is accompanied of alternating expulsion of  $\text{Cu}^0$  and insertion of  $\text{Cu}^{2+}$  during the reduction and oxidation, respectively. In this scenario, it is likely that upon reduction and release of Cu from the aluminate phase, the  $\text{Al}^{3+}$  of the defective Cu-less aluminate does not recover the  $\text{AlO}_4/\text{AlO}_6$  ratio of the initial aluminate. We therefore suggest that the Cu insertion and extraction from the spinel structure results in coordination change from tetra to octahedral Al throughout cycling.

Because the  $\text{Cu}_x\text{Al}_y\text{O}_4$  is relatively stable at this temperature and once formed should not undergo changes during the short oxidation period, we suggest that the alpha phase transition initiates locally from the Cu-less aluminate during the reduction steps.

### Connecting atomic to grain scale migration

Taking a closer look at the sample after 50 redox cycles at 900 °C where the OC is composed of all the possible Cu- $\text{Al}_2\text{O}_3$  phases, the various phenomena can be explained at two scales: at the atomic scale and at the microscopic scale.

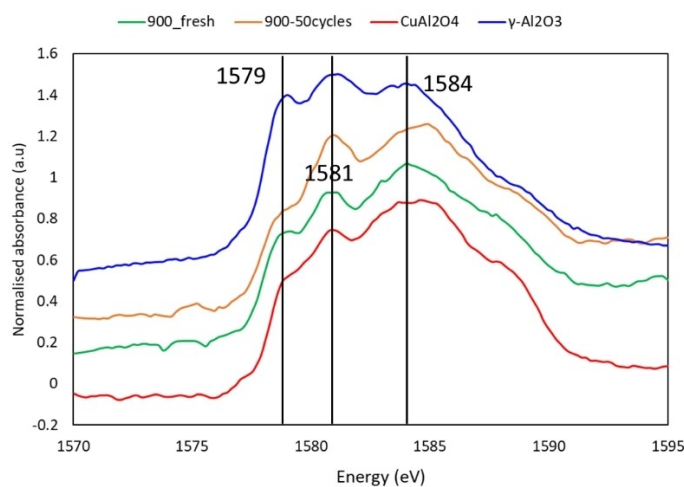


**Figure 10.** Al K-edge spectra of the CuO/ $\text{Al}_2\text{O}_3$ -900, CuO/ $\text{Al}_2\text{O}_3$ -900-after 50 cycles, CuO/ $\text{Al}_2\text{O}_3$ -900-after 200 cycles and  $\text{CuAl}_2\text{O}_4$ .



The schematic representation in Figure 11 displays the different events at both scales. Following the reduction of copper aluminate, the Cu atoms diffuse out of the Cu-aluminate to form metallic Cu nanoparticles supported on Cu-less aluminate via reaction Reduction 1.<sup>[31]</sup> Following the expulsion of copper and diffusion on support grain surfaces, copper particle sizes may grow via Particle Migration and Coalescence (PMC) and/or Ostwald Ripening (OR).<sup>[32]</sup> Upon reductive extraction of Cu, some Cu-less aluminate particles might undergo transition to alpha alumina phase which results in a rearrangement of support grains through progressive sintering and mesopore destruction at the benefit of larger macropores.

With the introduction of oxygen during an oxidizing cycle, metallic copper forms either CuO or  $\text{Cu}_x\text{Al}_y\text{O}_4$ . To carry out the reformation of  $\text{Cu}_x\text{Al}_y\text{O}_4$ , the Cu nanoparticles are redispersed at the surface of Cu-less aluminate by surface diffusion and within the spinel structure by vacancy filling or by Al substitution and further solid-state diffusion. Because of the stepwise alumina phase transition from spinel to HCP and the gradual increase of the  $\text{AlO}_4/\text{AlO}_6$  ratio of the structural Al, copper may reside on supports variably susceptible to reform Cu-aluminate. The ability for copper to reach a Cu-less aluminate site depends on the diffusion distance allowed within the temperature and time conditions of the oxidizing step. Consequently, only a fraction of the copper atoms has the freedom to jump towards a spinel site, while the remaining copper fraction is restricted to CuO particles in macroporous traps within the alpha alumina region. The stepwise migration of copper through the grain creates a

concentration gradient from higher concentration (at the interface) to lower concentration away from the interface into the “fresh” spinel region and into the  $\alpha\text{-Al}_2\text{O}_3$  region. As a result, some CuO gets stranded either due to diffusion distance or higher particle size, leading to larger CuO particles instead of Cu-aluminate. The morphology of the two-regions separating front is quite heterogeneous from one grain to another, calling for local controls on the initiation and propagation of the reaction. Strikingly, the migration of copper, and the related spinel to alpha-alumina phase transition, seem to initiate at discrete clusters within the grains, which act as centers for a radial Cu-concentration gradient. The origin of this discrete and localized phase transition may be related to stochastic clusters nucleation followed by growth process. This cyclic redox stepwise dynamic behaviour has to our knowledge never been described elsewhere. It is in some respects similar to self-crystallization propagating waves described in metallic melts or in hydrogels.

### Redox cycles at 800 °C

The summary of the XRD and XAS data of the  $\text{CuO}/\text{Al}_2\text{O}_3$ -800 series are presented in Table 3. After 50 redox cycles the sample contains CuO,  $\text{Cu}_x\text{Al}_y\text{O}_4$  and transition alumina. Compared to the fresh sample at 800 °C, the  $\text{Cu}_x\text{Al}_y\text{O}_4$  peaks appear sharper. The relative peak intensity of the CuO and the  $\text{Cu}_x\text{Al}_y\text{O}_4$  points to an increase in the aluminate percentage. Using XAS, we get a

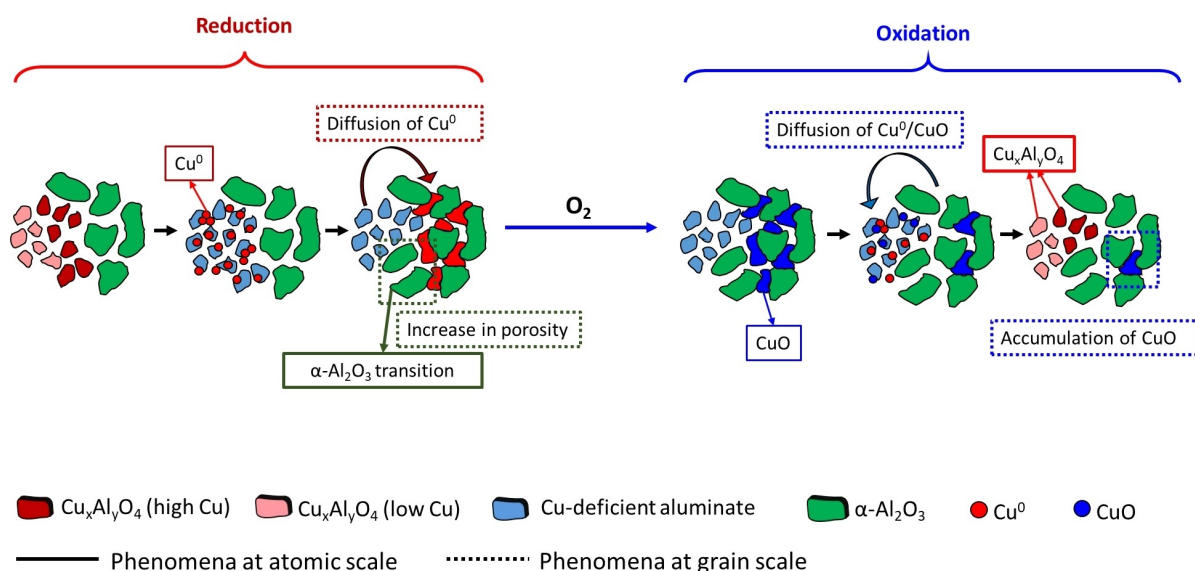


**Figure 11.** Schematic representation of the phase transitions, interactions and the migration of the copper species.

**Table 3.** Identification of the copper and alumina phases in the  $\text{CuO}/\text{Al}_2\text{O}_3$ -800 samples after 50 and 200 cycles at 800 °C from XRD (diffractograms presented in SI.3.2) and quantification of Cu species (% relative spectrum) by XAS (spectral fitting provided in SI.2.3).

	50 cycles	200 cycles
XRD	CuO, $\text{Cu}_x\text{Al}_y\text{O}_4$ , transition $\text{Al}_2\text{O}_3$	CuO, $\text{Cu}_x\text{Al}_y\text{O}_4$ , transition $\text{Al}_2\text{O}_3$ , $\alpha\text{-Al}_2\text{O}_3$
XAS–CuO: $\text{Cu}_x\text{Al}_y\text{O}_4$	23:77	42:58

relative amount of 23:77 for  $\text{CuO}:\text{Cu}_x\text{Al}_y\text{O}_4$  phases. Peaks corresponding to  $\delta\text{-Al}_2\text{O}_3$  are also observed, whereas they could not be discerned in the fresh sample due to the overlapping of the broadened peaks.

After 200 redox cycles at  $800^\circ\text{C}$ , the sample displays the presence of  $\text{Cu}_x\text{Al}_y\text{O}_4$ ,  $\text{CuO}$ , transition alumina and  $\alpha\text{-Al}_2\text{O}_3$ . In terms of transition aluminas, both  $\theta$  and  $\delta$  phases can be identified from the diffractogram. From the relative XRD peaks intensities related to  $\text{CuO}$  and  $\text{Cu}_x\text{Al}_y\text{O}_4$  phases, the  $\text{CuO}$  concentration seems to have increased compared to the sample after 50 cycles. The increase in  $\text{CuO}$  concentration was confirmed from XAS data with a ratio of 42:58 for the  $\text{CuO}:\text{Cu}_x\text{Al}_y\text{O}_4$  phases (Table 4).

The cross-section SEM images of the fresh sample, after 50 and 200 cycles are presented in Figure 12. The top and the bottom rows display the overview of the whole grain and the higher resolution images of the areas marked with red squares, respectively.

After 50 cycles, copper is distributed in different forms as observed in the SEM imaging (Figure 12, 50 cycles). The grains are composed of a dark grey matrix containing spherical areas ( $1\text{--}10\text{ }\mu\text{m}$  in diameter) with light grey contrast. The dark grey matrix (pink circle) is in the form of small agglomerates of homogeneously distributed particles made of several tens of nm with a Cu concentration of 5–8 wt%. In comparison, the

light grey areas (red circle) contain a higher concentration of copper (about 15 to 25 wt%). The particles in these zones are often denser and larger in size, compared to the particles in the grey matrix. Some porosity and cracks can be observed as well within these copper-rich spherical zones. Within some of these spheres some  $\text{CuO}$  particles of 20 to 500 nm size (circled in blue) are also noted. On the outer periphery of the grains, the Cu-rich phase is found either forming 5–10  $\mu\text{m}$  sized particles or a discontinuous layer of 1 to 2  $\mu\text{m}$  thickness. The copper to oxygen weight ratio is found to be about 80/20 wt%, pointing at the  $\text{CuO}$  phase. Between the white crust and grey matrix, a gradient is observed from high to lower copper concentration from the outer edge towards the center of the grain. The grey matrix formation is likely to be due to the inward diffusion of the large copper crystallites (seen in the fresh sample), induced by temperature during the cycling.

After 200 cycles, the sample displays similar features as that after 50 cycles. However, the spherical copper-rich areas have larger diameters ranging from 5 to 20  $\mu\text{m}$ . A larger number of cracks is also observed within, and outside of those spherical areas (Figure 12, 200 cycles). Within the cracks,  $\text{CuO}$  either fills the cracks continuously (few  $\mu\text{m}$ ) or exists as individual particles of 50–200 nm (marked in blue circle in Figure 12, 200 cycles). There is a Cu concentration gradient from the cracks to the matrix. The areas circled in red are often denser, with a copper

**Table 4.** Identification of the copper and alumina phases in the  $\text{CuO}/\text{Al}_2\text{O}_3$ -700 samples after 50 and 200 cycles at  $700^\circ\text{C}$  from XRD (diffractograms presented in SI.3.3) and quantification of Cu species (% relative spectrum) by Cu K edge XAS (spectral fitting provided in SI.2.4).

	50 cycles	200 cycles
XRD	$\text{CuO}$ , $\text{Cu}_x\text{Al}_y\text{O}_4$ , transition $\text{Al}_2\text{O}_3$	$\text{CuO}$ , $\text{Cu}_x\text{Al}_y\text{O}_4$ , transition $\text{Al}_2\text{O}_3$ , $\alpha\text{-Al}_2\text{O}_3$
XAS-CuO: $\text{Cu}_x\text{Al}_y\text{O}_4$	40:60	not evaluated

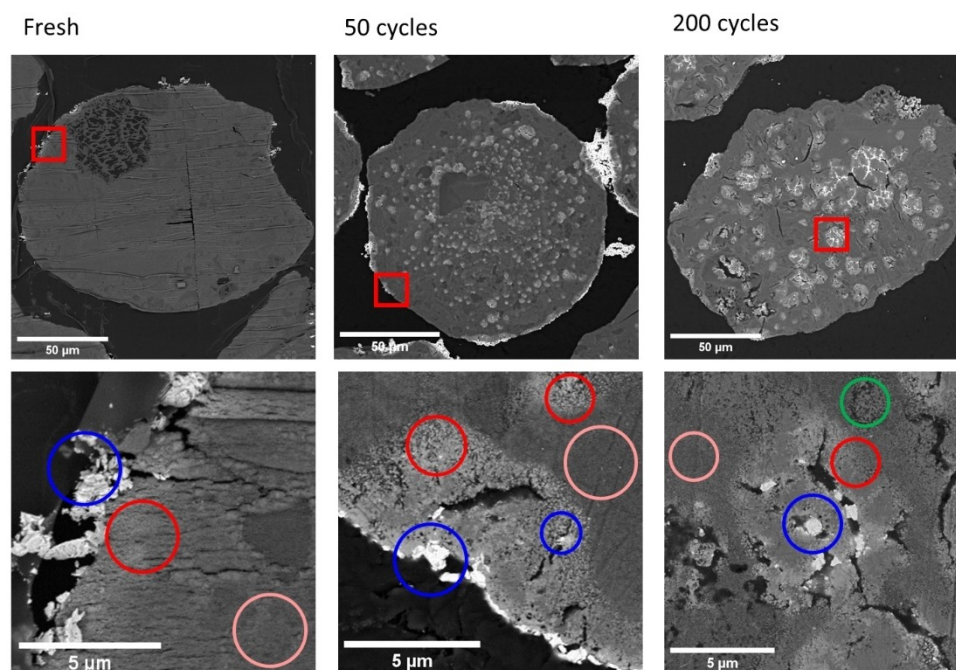


**Figure 12.** SEM image of the grains (top row) and the red square areas (bottom row) of the fresh sample, after 50 and 200 cycles at  $800^\circ\text{C}$ .

concentration of 10–25 wt%, attributed to the  $\text{Cu}_x\text{Al}_y\text{O}_4$  phase. Large crystallites or crusts of Cu-rich phase are still observed on the outskirts of the grain for this sample. Apart from the Cu-rich spheres, the sample contains a dark grey matrix, containing only 1–3 wt% Cu. The matrix in dark grey appears to be denser in some areas, and porous in some of the areas (green circle). The phase identification from XRD and the presence of different morphologies indicate the existence of different alumina polymorphs. While the denser areas might be made of the transition aluminas ( $\delta$  and  $\theta$ ), the porous areas with larger particles (marked with a blue circle) exhibit a morphology resembling that of the  $\alpha$ -alumina phase. At the periphery of the grains, crystals of a few hundred nm to a few  $\mu\text{m}$  can be found, likely to be composed of CuO.

From the fresh sample to the 50 cycled sample, there is a slight increase in the amount of the  $\text{Cu}_x\text{Al}_y\text{O}_4$  phase, plausibly due to the incorporation of the peripheral CuO into the support grain. However, further cycling leads to a decrease in the amount of  $\text{Cu}_x\text{Al}_y\text{O}_4$  and an increase in CuO. This phenomenon can be attributed to the emergence of the  $\alpha$ - $\text{Al}_2\text{O}_3$  phase, similar to that observed in the  $\text{CuO}/\text{Al}_2\text{O}_3$ -900 series.

## Redox cycles at 700 °C

Based on literature, SEM and XAS characterizations, the  $\text{CuO}/\text{Al}_2\text{O}_3$ -700 fresh material sample is composed of the same species as  $\text{CuO}/\text{Al}_2\text{O}_3$ -800 material. However, due to the diffusion-controlled nature of the reaction between CuO and  $\text{Al}_2\text{O}_3$ , at a lower temperature of calcination it is expected to have a higher proportion of unreacted CuO. After being subjected to 50 redox cycles at 700 °C, the oxygen carrier

displays the presence of copper oxide, copper aluminate ( $\text{Cu}_x\text{Al}_y\text{O}_4$ ) and transition alumina, according to XRD data (Supplementary information). The linear combination fitting of the Cu-K edge XAS data provides a proportion of 40:60 for  $\text{CuO}:\text{Cu}_x\text{Al}_y\text{O}_4$  phase content ratio. No alpha alumina is observed either from XRD or SEM characterizations.

After 200 cycles at 700 °C, the material is composed of copper aluminate, CuO and  $\alpha$ - $\text{Al}_2\text{O}_3$  according to the X-Ray diffractograms (Supplementary information). The peaks corresponding to the  $\text{Cu}_x\text{Al}_y\text{O}_4$  phase appear to be significantly sharper with higher intensity than the sample after 50 redox cycles. Additionally, the position of the aluminate peaks appears to be closer to that of the stoichiometric  $\text{CuAl}_2\text{O}_4$  phase. Gradually, more Cu was incorporated in the aluminate at the expense of CuO, while the remaining alumina turned into the alpha phase.

The cross-section SEM images of the fresh sample, after 50 and 200 cycles at 700 °C are presented in Figure 13. The top and the bottom rows display the overview of the whole grain and the higher resolution images of the areas marked with red squares, respectively.

The fresh sample resembles that of the fresh sample calcined at 800 °C, with larger crystallites of CuO on the outer edge of the OC grains.

After 50 cycles, the oxygen carrier appears to be composed of a copper-rich grain edge with large CuO crystals. The interior of the grain contains a matrix of alumina with a very small percentage of copper (< 2 wt%). As observed in the STEM-EDS map (SI.5.5), the matrix is composed of small particles containing a mixture of Cu–Al species. The matrix is likely to be made of non-stoichiometric aluminate-transition alumina mixture. In this matrix some dispersed copper-based particles (30–

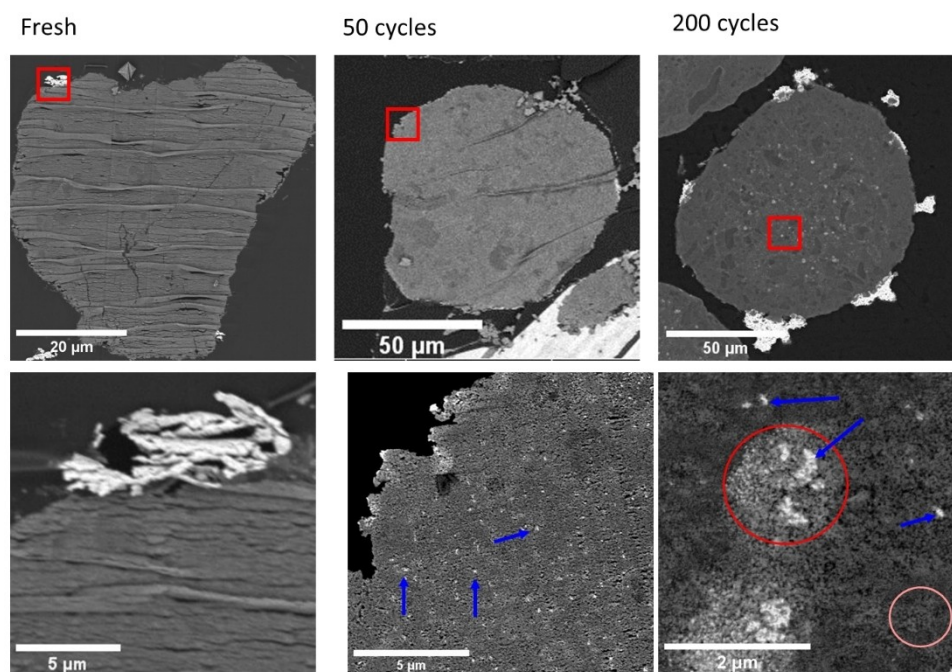


**Figure 13.** SEM image of the grains (top row) and the red square areas (bottom row) of the fresh sample, and after 50 and 200 cycles at 700 °C.



100 nm) and large aggregates of copper-based particles (1–3  $\mu\text{m}$ ) are observed according to Figure 13. In some areas in the matrix, large pores of 50–100 nm are noted. The Cu–Al matrix appears to be larger in size in the porous areas compared to the compact areas. Particle sintering could lead to the formation of large porosity in those areas. The exact composition of the Cu-rich aggregates could not be discerned since they are either found on or close to the alumina matrix, thus contribution of Al is inevitable in the EDS analysis. However, from the morphology and concentration of the particles, they are likely to be CuO crystallites.

Figure 13 displays the overall changes in the morphology and copper distribution after 200 cycles at 700 °C. In the interior of the grain four different features are noted. The zone circled in red depicts spherical regions of 1–2  $\mu\text{m}$  diameter, with a 6–8 wt% copper concentration. Inside these spherical regions the presence of some dense particles (pointed with blue arrow) with 15–30 wt% copper is also noted, possibly composed of agglomeration of CuO particles. Within the grey matrix the blue arrows point to single particles of 60–200 nm in diameter, likely to be made of CuO. Moreover, areas with higher porosity are observed within the matrix, as indicated by the pink circle in the same image. From the contrast, the presence of porosity, and the absence of copper, these areas are presumed to be  $\alpha\text{-Al}_2\text{O}_3$  phase. Some large particles of 5–20  $\mu\text{m}$  CuO are noticed at the edge of the grain. Similarly to the sample calcined at 800 °C, a copper concentration gradient is observed which follows a higher concentration (30–40 wt%) to a lower concentration following the edge to the interior of the grain.

The multiple redox cycling of the sample at 700 °C led to an overall increase in the particle size range of the copper phase compared to the fresh sample. In terms of microstructure, the size of the Cu-rich spherical areas appears to increase with the number of cycles. The quantitative analysis of the XAS spectra displayed a slight increase in the relative percentage of  $\text{Cu}_x\text{Al}_y\text{O}_4$  phase from 55% in the fresh sample to 60%, after 50 cycles. Unfortunately, the relative percentage in the sample after 200 cycles could not be estimated as XAS was not performed on this sample. However, from the XRD data and SEM data it can be deduced that the relative percentage of the  $\text{Cu}_x\text{Al}_y\text{O}_4$  phase has increased. Furthermore, the porous structure in some areas could be linked to the formation of the  $\alpha\text{-Al}_2\text{O}_3$  phase which is confirmed by XRD. Surprisingly, the alpha formation occurred at temperatures as low as 700 °C.

## Effect of reaction temperature and number of cycles

The phase evolution and the resulting morphology of the oxygen carriers depend on the number of redox cycles. Moreover, the temperature of the reaction is a predominant factor. At 900 °C, copper aluminate formation is dominant (before the emergence of  $\alpha\text{-Al}_2\text{O}_3$ ). In comparison, at lower calcination temperatures (700 or 800 °C), both CuO sintering and Cu-aluminate formation take place. The calcination temperature

defines the initial state of the material and the migration mechanisms which eventually determine the evolution of the different phases. Presumably, there is a competition among different migration processes. In one case, bulk diffusion and solid-state reaction lead to the formation of the aluminate phase. In another case sintering occurs due to surface or grain boundary migration. At 900 °C, the bulk diffusion is generally more prominent resulting in the formation of copper aluminate phase. On the contrary, at 700 °C, surface or grain boundary migration is prominent, leading to larger CuO crystallites as a function of the number of cycles. This interpretation is further corroborated by following the redox cycling of an initial CuO/ $\text{Al}_2\text{O}_3$ -900 sample at 700 °C by *in situ* XRD (presented in details in SI.4.2). The initial sample containing  $\text{Cu}_x\text{Al}_y\text{O}_4$  as the only copper-containing phase gradually transforms to CuO as a result of cycling at a “low” temperature. At 800 °C, there is competition between both phenomena, and strong CuO sintering as well as microstructural changes in the support grain are observed.

The schematic representation displayed in Figure 14 gives an overview of the global effect of temperature and the number of redox cycles. During oxidation, migration of the copper phases can either lead to sintering and formation of large CuO particles via surface or grain-boundary diffusion, or to the formation of non-stoichiometric  $\text{Cu}_x\text{Al}_y\text{O}_4$  spinel via solid-state reaction between copper oxide and alumina. At lower temperatures ( $\leq 800$  °C), the surface or grain-boundary diffusion is dominant, and cumulated redox cycling of the oxygen carrier results in the dispersion of large CuO particles within the Cu-containing alumina grains. At higher temperatures ( $\geq 900$  °C), the non-stoichiometric  $\text{Cu}_x\text{Al}_y\text{O}_4$  spinel formation is dominant, and CuO reacts with alumina to form Cu-aluminate phase. While the oxidative formation of spinel is favorable in the CuO + transition alumina system, it is kinetically limited in the case of CuO +  $\alpha\text{-Al}_2\text{O}_3$ . Hence, with an increasing number of cycles,  $\alpha$ -alumina and CuO phases segregate and eventually large CuO crystals are formed within a porous  $\alpha$ -alumina support. At 900 °C, the  $\alpha\text{-Al}_2\text{O}_3$  phase transition is responsible for the dramatic morphology change in the oxygen carrier. As it turns out, the presence of copper tends to promote the  $\alpha\text{-Al}_2\text{O}_3$  formation, likely from Cu-deficient aluminate during reduction. It is speculated that copper contributes to the local structural organization leading to a higher proportion of octahedral Al–O environments compared to transition aluminas. Since, the  $\alpha\text{-Al}_2\text{O}_3$  phase is composed of octahedrally coordinated  $\text{Al}^{3+}$  ions, a slight change in the local bonding environment in the aluminate may reduce the overall phase transition energy barrier. Consequently, instead of following the conventional  $\gamma \rightarrow \delta \rightarrow \theta \rightarrow \alpha\text{-Al}_2\text{O}_3$  transition sequence (which generally occurs above 1000 °C), the copper-induced structural change may lead to the direct transition to  $\alpha\text{-Al}_2\text{O}_3$  at a lower temperature.

## Conclusion

The current study demonstrates how powerful the combination of multi-scale imaging techniques is to reveal the interactions



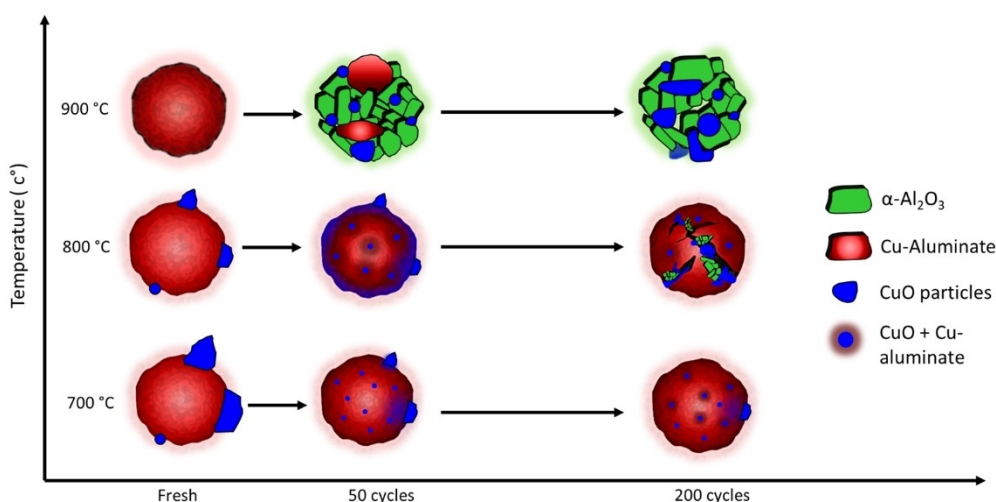


**Figure 14.** Schematic diagram depicting the phase and morphological evolution of the CuO- $\text{Al}_2\text{O}_3$  oxygen carrier under oxidized form, as a function of reaction temperature and the number of reduction-oxidation cycles.

of metal/metal oxides and ceramic supports in complex and heterogeneous reactive systems. A correlative spectro-microscopic (SEM, STEM-EDX and STXM-XAS) approach was used to understand how the evolution of both Cu and alumina-based phases and their interaction after different ageing durations under successive redox cycles are linked to copper migration inside the alumina grain. While the coupled STXM-XAS provided information on the local chemical environment in the form of a chemical map of the fresh and aged CuO/ $\text{Al}_2\text{O}_3$  oxygen carriers, STEM-EDS allowed higher resolution imaging to determine morphological characteristics and spatial distribution of copper-based species. A comprehensive mechanism is proposed concerning the redox behavior of the CuO/ $\text{Al}_2\text{O}_3$  system, relating the diffusion of the Cu-species, the active phase-support interactions and the role of copper in the  $\text{Al}_2\text{O}_3$  support phase transition to the temperature and the number of cycles. Three competitive and interconnected phenomena are involved: (i) competition between CuO and  $\text{Cu}_x\text{Al}_y\text{O}_4$  phases formation, which is driven by reaction temperature and duration as well as the alumina phase in presence, (ii) particle size growth of CuO during the reduction/oxidation cycles and (iii) phase transition to  $\alpha\text{-Al}_2\text{O}_3$  which is promoted by the presence of copper and the reaction temperature. In particular, we report a process whereby the mobility of copper is driven by the phase transition from FCC spinel to HCP  $\alpha\text{-Al}_2\text{O}_3$  during the course of redox cycling. Following the formation of the  $\alpha\text{-Al}_2\text{O}_3$  phase, some of the copper tend to form segregated areas composed of CuO supported on  $\alpha\text{-Al}_2\text{O}_3$  while the rest of the copper reacts with the remaining spinel-support to reform Cu-aluminate. This mechanism provokes a series of reaction fronts that sweep across the macroscopic grains and control the kinetics and three-dimensional distribution of texture and phase distribution, both controlling the overall performance of the oxygen carrier grain.

These new insights could help to identify ways to design more stable oxygen carriers e.g., by doping the alumina

support with aliovalent cations to prevent the  $\alpha\text{-Al}_2\text{O}_3$  transition, or to stabilize the  $\text{Cu}_x\text{Al}_y\text{O}_4$  phase. Understanding the ageing process, the chemical and structural variation within oxygen carrier materials is imperative to elucidate the structure–function relationships and ultimately paves a way to design more stable oxygen carriers.

## Materials and Methods

### Material Preparation

OC materials containing 13 wt% CuO over  $\text{Al}_2\text{O}_3$  support have been prepared according to a protocol adapted from Abad et al. with few modifications to the temperature and duration of calcination.<sup>[10]</sup> An aqueous solution of copper nitrate ( $\text{Cu}(\text{NO}_3)_2 \cdot 5\text{H}_2\text{O}$ ) (from Sigma Aldrich) corresponding to the total pore volume of the support ( $\gamma\text{-Al}_2\text{O}_3$ , Puralox SCFa series from Sasol) is slowly added to the support grains at room temperature under constant stirring. Afterwards, the mixture is kept aside for a 3 hours period of maturation in a humid atmosphere at room temperature. Later, the mixture is dried overnight at a temperature of 120 °C. Finally, the impregnated supports are calcined at 700, 800 or 900 °C for 12 hours to produce the supported oxygen carrier. The fresh samples are called CuO/ $\text{Al}_2\text{O}_3\text{-T}$  where the T is the temperature of calcination.

### Material Ageing

A thermogravimetric analysis (TGA) device was used to carry out the ageing of the oxygen carrier materials. The TGA device used in this study is a symmetric SETARAM TAG 24 thermobalance.

During a typical run, 20–30 mg of sample is placed in a Pt crucible. To avoid temperature fluctuation and overheating of

the furnace, the sample is heated under air in two stages: at a rate of 40 °C/min from room temperature to 100 °C below the temperature set point, and then at 10 °C/min up to the reaction temperature. Materials reaction and ageing is operated by redox cycles with alternating reducing (10% H<sub>2</sub>, 90% N<sub>2</sub>) and oxidizing (air) gases for 3 minutes under each gas. To avoid mixing of H<sub>2</sub> and air, the TGA system is purged under N<sub>2</sub> gas flow (for 1.5 minutes) in between the reduction and oxidation steps. The flowrate of the gases are set to 150 mL/min.

A temperature of 700, 800 or 900 °C was used to probe the effect of the reaction temperature and number of cycles (50 and 200 cycles) on the ageing of the oxygen carriers. Each sample was previously calcined at the same temperature as the ageing test.

It should be noted that TGA is not representative of circulating fluidized bed conditions, and it is likely that pushing materials conversion to its maximum might contribute to a higher chemical stress for the material (and therefore accelerated ageing).

## Characterization techniques

### Scanning Electron Microscopy

SEM imaging with semi-quantitative elemental analysis is performed on FEI Nova nanoSEM 450 apparatus equipped with Oxford XMAX 80 EDS detector operating at 15 KeV. The polished cross-section samples were prepared by embedding the grains of CuO/Al<sub>2</sub>O<sub>3</sub> in epoxy resin and polished with SiC sheet.

### Scanning Transmission Electron Microscopy

The STEM experiments were mainly carried out using JEOL JEM-2100F microscope operating at 200 kV voltage. The microscope is equipped with an electronic probe corrector to correct the spherical aberration of the condenser lens, high resolution objective lens pole piece and an UltraScan 1000 CCD array detector from Gatan. Elemental analysis was performed using Energy Dispersive X-ray Spectroscopy (EDS) probe equipped with silicon drift detector (SDD) with a sensor size of 60 mm<sup>2</sup>.

### X-ray Diffraction

XRD characterizations were performed using a PANalytical X'Pert Pro Diffractometer in Bragg-Brentano configuration with Cu K $\alpha$  radiation ( $\lambda = 1.54$  nm) fitted with X'Celerator detector.

For the data acquisition the samples were ground into powder and compacted in a sample holder. An angle range of 5° to 70° 2 $\theta$  with a step size of 0.033°, dwell time of 500 s/step were set for the measurements.

The assignments of the crystalline phases were carried out using DIFFRAC.EVA software supported by Crystallographic Open database (COD). The following crystallographic informa-

tion files were used for the phase identifications: Powder diffraction files, PDF 03-065-9026 for metallic copper, PDF 04-007-9767 for Cu<sub>2</sub>O, PDF 00-010-0425 for gamma alumina, PDF 04-007-0518 for CuO, PDF 04-015-0578 for CuAl<sub>2</sub>O<sub>4</sub>, PDF 00-035-1401 for CuAlO<sub>2</sub> and PDF 01-070-5679 for alpha alumina

### In-situ X-ray Diffraction

The *in situ* XRD experiments were conducted using the apparatus "XRK 900" from Anton Paar. For the data acquisition the samples were ground into powder and compacted in a special reactor bed. The data acquisition was carried out in the 30–50° 2 $\theta$  range with a step size of 0.033 °C and 50 s/step. One diffractogram acquisition took 4 min. To carry out oxidation and reduction cycles, air and H<sub>2</sub> (100 vol%) with a flow rate of 2 L/hour and 1 L/hour were used, respectively. The mixing of the two gases was avoided by purging the system with N<sub>2</sub> in between the two reactions. With this reactor setup, it is possible to reach a temperature of 700 °C under hydrogen and a temperature of 1000 °C under N<sub>2</sub> and air.

### Scanning Transmission X-ray Microscopy–X-ray Absorption Near Edge Spectroscopy

The STXM analyses were carried out on the HERMES beamline of the SOLEIL synchrotron.<sup>[15]</sup> The energy range of the HERMES beamline is particularly advantageous to probe both copper and aluminum chemical coordination, thus providing a complete picture of the sample's local environments.

STXM is a spectro-microscopic technique comprising a combination of spatially resolved spectroscopy and imaging with spectral sensitivity. The STXM image is obtained in raster mode recording the transmitted X-ray intensity while scanning the sample. Each pixel intensity follows the Beer-Lambert law linking the recorded intensity to the impinging one through an exponential decay as a function of the sample thickness,  $d$ , density,  $\rho$ , and energy dependent linear absorption coefficient,  $\mu(E)$ . To focus the soft X-ray beam, a diffractive Fresnel Zone Plate (FZP) is used. A beam-stop of 80  $\mu$ m and an order sorting aperture (OSA) of 50  $\mu$ m are used to filter only the first diffracted order. For these experiments we used a 35 nm outermost FZP giving a beam spot size in the focus of  $\sim 43$  nm, relevant for the expected spatial resolution. All measurements were carried out using circularly polarized X-ray beam such as to elude possible artefacts arising from linear anisotropies, and at normal incidence with respect to the sample.

The samples for STXM experiments were prepared using ultramicrotomy sectioning on capsules of impregnated powders in TEM resin to a thickness of 100 nm and placed on Ni (75 mesh, carbon+formvar coated) TEM grids. Energy stacks and mappings were performed at the Cu L<sub>3</sub>-edge (932 eV) and Al K-edge (1559 eV). The air-sensitive samples were prepared in a glove box and sealed in-between two SiN membranes of 30 nm thickness.

The copper- and alumina-based reference samples were simply ground and drop-casted using a solvent carrier on the Ni-grid. The copper-based phases present in OC are composed of Cu<sup>0</sup>, Cu<sub>2</sub>O, CuO, CuAl<sub>2</sub>O<sub>4</sub>, and CuAlO<sub>2</sub>. In terms of Cu reference samples, Cu<sup>0</sup>, CuO and CuAl<sub>2</sub>O<sub>4</sub> were analysed. At the time of the experimental run, pure CuAlO<sub>2</sub> compound had not been synthesized. Similarly, the spectrum of the Cu<sub>2</sub>O sample could not be obtained due to inadequate sample preparation. Nevertheless, the absence of Cu<sub>2</sub>O or CuAlO<sub>2</sub> in the reference database did not affect the data treatment protocol. The oxidized samples contained CuO and CuAl<sub>2</sub>O<sub>4</sub>. The reduced samples were composed of only metallic Cu, as deduced from the post-mortem analysis. For alumina phases, three references were considered: α-Al<sub>2</sub>O<sub>3</sub>, γ-Al<sub>2</sub>O<sub>3</sub>, and CuAl<sub>2</sub>O<sub>4</sub>. Other transition aluminas were not taken into account due to difficulties to acquire pure phases, and as most often these phases exist as mixtures.<sup>[20,25]</sup>

The data analysis was carried out using AXIS2000 software.<sup>[33]</sup> Details of the data acquisition and analysis are provided in the supplementary information SI.1.

### X-ray Absorption Spectroscopy

The quick XAS experiments were carried out at the ROCK beamline at the SOLEIL synchrotron.<sup>[34]</sup> The data acquisitions were carried out at Cu K-edge (8989 eV), collected in transmission mode using three ionization chambers filled with nitrogen gas. The first ionization chamber was used to measure the intensity of the incident beam, the second one the intensity transmitted by the sample and the third one was dedicated to collect transmission data from a reference copper foil used for correcting possible energy drift of the monochromator during the experiment. As a post-treatment, the inflection point of the Cu foil used as reference is set to 8979 eV. The temporal resolution per spectrum was set to 250 ms with the collection of 4 spectra per second, i.e. 2 spectra with increasing Bragg angles of the Si(111) channel-cut monochromator and 2 spectra with decreasing Bragg angles. An average of 1800 spectra recorded with increasing Bragg angles (equivalent to 15 min of acquisition) was achieved to obtain a good signal to noise ratio.

The samples were ground, and 7 to 15 mg of powders were mixed with boron nitride to form pellets of 1.3 cm<sup>2</sup> in order to achieve an optimized edge jump around 1.0.

The spectra were fitted with a linear combination fitting (LCF) algorithm, using CuO and non-stoichiometric copper aluminate (Cu<sub>x</sub>Al<sub>y</sub>O<sub>4</sub>) as reference spectra using the Athena(D) software.<sup>[35]</sup> All the information on the reference spectra and the spectral fitting are provided in SI.2.

### Acknowledgements

The authors are thankful to the Direction of Physics and Analysis at IFP Energies Nouvelles for the XRD and SEM characterizations. The work at ROCK was supported by a public grant overseen by the French National Research Agency (ANR) as part of the

Investissements d'Avenir program (reference: ANR10-EQPX45). We acknowledge SOLEIL synchrotron facility for providing beamtime under project number 20190320 and 20201423 for access to HERMES and ROCK beamlines, respectively.

### Conflict of Interest

The authors declare no conflict of interest.

### Data Availability Statement

The data that support the findings of this study are available from the corresponding author upon reasonable request.

**Keywords:** copper migration · CuO/Al<sub>2</sub>O<sub>3</sub> · phase transition · STXM-XANES · TEM

- [1] Intergovernmental Panel on Climate Change. *Climate Change 2021. The Physical Science Basics*, Intergovernmental Panel on Climate Change. 2021 <https://www.ipcc.ch/report/ar6/wg1/chapter/chapter-2/#ccb-2.3>.
- [2] T. Stocker, Ed., *Climate change 2013: The physical Science Basis: Working Group I contribution to the Fifth assessment report of the Intergovernmental Panel on Climate Change*, Cambridge University Press, New York, 2014, pp 119–158.
- [3] *Energy Technology Perspectives International Energy Agency* 2017, pp 161–212
- [4] M. Ishida, H. Jin, *J. Chem. Eng. Jap.* **1994**, 27, 296–301.
- [5] A. Lyngfelt, *Energy Fuels* **2020**, 34, 9077–9093.
- [6] L. Protasova, F. Snijders, *Fuel* **2016**, 181, 75–93.
- [7] A. Lambert, A. Tilland, W. Pelletant, S. Bertholin, F. Moreau, I. Clemençon, M. Yazdanpanah, *Fuel* **2018**, 216, 71–82.
- [8] A. Abad, J. Adáñez, F. García-Labiano, L. F. De Diego, P. Gayán, J. Celaya, *Chem. Eng. Sci.* **2007**, 62, 533–549.
- [9] L. F. De Diego, F. García-Labiano, P. Gayán, J. Celaya, J. M. Palacios, J. Adáñez, *Fuel* **2007**, 86, 1036–1045; a-Labiano, P. Gayán, J. Celaya, J. M. Palacios, J. Adáñez, *Fuel* **2007**, 86, 1036–1045.
- [10] L. F. De Diego, P. Gayán, F. García-Labiano, J. Celaya, A. Abad, J. Adáñez, *Energy Fuels* **2005**, 19, 1850–1856.
- [11] M. Pishahang, Y. Larring, R. E. Stensrød, K. A. Andreassen, A. I. Spjelkavik, *Int. J. Greenhouse Gas Control* **2021**, 109, 103384.
- [12] M. T. Izquierdo, F. García-Labiano, A. Abad, A. Cabello, P. Gayán, L. F. De Diego, J. Adáñez, *Fuel Process. Technol.* **2021**, 215, 106740.
- [13] C. R. Forero, P. Gayán, F. García-Labiano, L. F. De Diego, A. Abad, J. Adáñez, *Int. J. Greenhouse Gas Control* **2011**, 5, 659–667.
- [14] A. Cabello, A. Abad, M. T. Izquierdo, P. Gayán, L. F. De Diego, F. García-Labiano, J. Adáñez, *Chem. Eng. J.* **2022**, 430, 132602.
- [15] M. Gironi, J. B. Goedkoop, R. Schoorl, F. M. F. De Groot, J. C. Fuggle, F. Schäfers, E. E. Koch, G. Rossi, J.-M. Esteve, R. C. Karnatak, *Phys. Rev. B* **1989**, 39, 1541–1545.
- [16] A. Sharma, M. Varshney, J. Park, T.-K. Ha, K.-H. Chae, H.-J. Shin, *RSC Adv.* **2015**, 5, 21762–21771.
- [17] K. Shimizu, H. Maeshima, H. Yoshida, A. Satsuma, T. Hattori, *Phys. Chem. Chem. Phys.* **2000**, 2, 2435–2439.
- [18] X. Ye, J. E. Schmidt, R. Wang, I. K. Ravenhorst, R. Oord, T. Chen, F. Groot, F. Meirer, B. M. Weckhuysen, *Angew. Chem. Int. Ed.* **2020**, 59, 15610–15617; *Angew. Chem.* **2020**, 132, 15740–15747.
- [19] J. Everett, F. Lermyte, J. Brooks, V. Tjendana-Tjhin, G. Plascencia-Villa, I. Hands-Portman, J. M. Donnelly, K. Billimoria, G. Perry, X. Zhu, P. J. Sadler, P. B. O'Connor, J. F. Collingwood, N. D. Telling, *Sci. Adv.* **2021**, 7, eabf6707.
- [20] Y. Kato, K. Shimizu, N. Matsushita, T. Yoshida, H. Yoshida, A. Satsuma, T. Hattori, *Phys. Chem. Chem. Phys.* **2001**, 3, 1925–1929.
- [21] D. Cabaret, Ph. Sainctavit, Ph. Ildefonse, A.-M. Flank, *J. Electron Spectrosc. Relat. Phen.* **1996**, 79, 21–24.

- [22] A. B. Altman, C. D. Pemmaraju, S. Alayoglu, J. Arnold, C. H. Booth, A. Braun, C. E. Bunker, A. Herve, S. G. Minasian, D. Prendergast, D. K. Shuh, T. Tylliszczak, *Inorg. Chem.* **2017**, *56*, 5710–5719.
- [23] K. Sohlberg, S. J. Pennycook, S. T. Pantelides, *Chem. Eng. Commun.* **2000**, *181*, 107–135.
- [24] M. Ozawa, H. Toda, P. Kato, S. Suzuki, *Appl. Catal. B* **1996**, *8*, 123–140.
- [25] A. Boumaza, L. Favaro, J. Lédion, G. Sattonnay, J. B. Brubach, P. Berthet, A. M. Huntz, P. Roy, R. Tétot, *J. Solid State Chem.* **2009**, *182*, 1171–1176.
- [26] S. T. Murphy, C. A. Gilbert, R. Smith, T. E. Mitchell, R. W. Grimes, *Philos. Mag.* **2010**, *90*, 1297–1305.
- [27] B. Hallstedt, *J. Am. Ceram. Soc.* **1992**, *75*, 1497–1507.
- [28] W. Hu, F. Donat, S. A. Scott, J. S. Dennis, *RSC Adv.* **2016**, *6*, 113016–113024.
- [29] K. Okada, A. Hattori, T. Taniguchi, A. Nukui, R. N. Das, *J. Am. Ceram. Soc.* **2004**, *83*, 928–932.
- [30] I. Levin, D. Brandon, *J. Am. Ceram. Soc.* **2005**, *81*, 1995–2012.
- [31] S. Sharna, A. Lambert, V. Rouchon, C. Legens, A.-L. Taleb, S. Stanesco, D. Chiche, A.-S. Gay, O. Ersen, *Microsc. Microanal.* **2021**, *27*, 57–58.
- [32] S. Sharna, M. Bahri, C. Bouillet, V. Rouchon, A. Lambert, A.-S. Gay, D. Chiche, O. Ersen, *Nanoscale* **2021**, *13*, 9747–9756.
- [33] Xis2000. <http://unicorn.mcmaster.ca/aXis2000.html>.
- [34] V. Briois, C. La Fontaine, S. Belin, L. Barthe, T. Moreno, V. Pinty, A. Carcy, R. Girardot, E. Fonda, *J. Phys. Conf. Ser.* **2016**, *712*, 012149.
- [35] B. Ravel, M. Newville, *J. Synchrotron Radiat.* **2005**, *12*, 537–541.

---

Manuscript received: October 24, 2022  
Revised manuscript received: December 15, 2022  
Version of record online: January 24, 2023